Chemical Engineering Journal 417 (2021) 129210

Contents lists available at ScienceDirect

Chemical Engineering Journal

journal homepage: www.elsevier.com/locate/cej

A pore-network-based upscaling framework for the nanoconfined phase behavior in shale rocks

Sidian Chen [a], Jiamin Jiang [b], Bo Guo [a,*]

[a] Department of Hydrology and Atmospheric Sciences, University of Arizona, Tucson, AZ 85721, USA
[b] Chevron Energy Technology Co., 1500 Louisiana St., Houston, TX 77002, USA

ARTICLE INFO

Keywords:
Nanopore networks
Capillary pressure
Adsorption
Condensate
Liquid-rich shale reservoirs

ABSTRACT

The presence of extensive nanopores in organic-rich shale introduces unique thermodynamic fluid phase behaviors owing to large pressure differentials across fluid-fluid interfaces and strong fluid-wall interactions. While the nanoconfined phase behavior has been extensively studied in a single nanopore, its manifestation in complex nanopore networks remains poorly understood and rigorously derived macroscopic phase behavior formulations are not yet available. We develop a novel upscaling framework for deriving macroscopic phase behavior formulations in realistic nanopore networks (e.g., obtained from high-resolution digital images of shale samples). The framework employs a generalized phase equilibrium model that explicitly accounts for the impact of capillary pressure and multicomponent adsorption in each pore. Assuming thermodynamic equilibrium across the pore network, macroscopic phase behavior variables for the entire pore network are then derived by integrating the variables from the individual pores. This leads to a macroscopic network-scale phase equilibrium model that naturally accounts for the size- and geometry-dependent nanoconfinement effects of a complex pore structure. Simulated phase behaviors using three multiscale pore networks demonstrate that (1) the phase behavior in a pore network—controlled by the multiscale pore structure—significantly deviates from that in a single nanopore and (2) due to capillary trapping of the liquid phase and competitive adsorption on the pore wall, heavier components tend to reside in smaller pores and suppress the bubble point pressure therein. The upscaled phase behavior model shares the same mathematical structure as that of a standard phase behavior model and can thus be readily incorporated in commercial reservoir simulators.

1. Introduction

Hydrocarbon recovery from liquid-rich shale reservoirs has grown rapidly in the past decade and reshaped the global energy landscape [1]. The abnormal phase behavior of hydrocarbon mixtures in shale rocks, i.e., significant deviation from that of the bulk fluids, poses unique challenges in predicting recovery rates from liquid-rich shale reservoirs [2–6]. Improving the predictive capability of reservoir simulations requires a comprehensive understanding of phase behaviors in the complex nanopore networks of shale rocks.

In nanoconfined pore spaces, large pressure differential across the fluid-fluid interfaces and strong interaction between fluid molecules and the pore wall make the phase behavior of a hydrocarbon mixture deviate from its bulk behavior [7–10]. These so-called nanoconfinement effects have been investigated by (1) nanofluidic experiments that directly measure the phase behavior in an individual nanopore [11–18] or a network of pores [19,20], and (2) theoretical models, such as molecular dynamics (MD) simulations [e.g., 21–23], grand canonical Monte Carlo (GCMC) or Gibbs ensemble Monte Carlo (GEMC) methods [e.g., 24–26], and density functional theory (DFT) [e.g., 27,28]. The theoretical models have been applied to simulate the phase behavior in pores that have different geometries (e.g., slit, cylindrical, ink-bottle, wedged shapes), sizes, and solid surface properties [27,29–31]. Collectively, the nanofluidic experimental [15] and advanced theoretical modeling studies [e.g., 22,26,32–35] have clearly demonstrated that nanoconfinement significantly modifies the fluid phase behavior and the multiscale pore structure is a primary factor that controls the overall phase behavior of a fluid mixture.

However, the new nanoconfined phase behaviors—revealed by the fundamental nanofluidic experiments and theoretical models—are yet to be incorporated in reservoir simulations that are routinely used for predicting and optimizing hydrocarbon productions in the field. Standard reservoir simulations often employ the so-called phase equilibrium models to simulate fluid phase behaviors. A phase equilibrium model treats each fluid phase as a continuum and assumes thermodynamic

* Corresponding author.
E-mail address: boguo@arizona.edu (B. Guo).

https://doi.org/10.1016/j.cej.2021.129210
Received 11 January 2021; Received in revised form 25 February 2021; Accepted 26 February 2021
Available online 3 March 2021

equilibrium between different fluid phases under isothermal conditions, i.e., the chemical potential or fugacity of each component is equal in different fluid phases for any prescribed temperature [36,37]. The standard phase equilibrium models do not directly apply to fluids confined in nanopores due to large pressure differentials across the fluid-fluid interfaces and strong fluid-solid interactions under nanoconfinement [9,14,38,39].

A number of studies have extended the phase equilibrium models to account for the nanoconfinement effects for a single nanopore. The effect of pressure differentials across the fluid-fluid interfaces (i.e., capillary pressure) can be modeled by assigning different pressures to the different fluid phases when computing the fugacities [3,40–44]. Because these models account for the capillary pressure only in a single pore, we refer to them as individual-pore phase equilibrium model. Employing such an individual-pore phase equilibrium model, Stimpson and Barrufet [45] investigated the impact of nanoconfinement on the relative permeability using a bundle-of-tubes model. Wang et al. [46] applied the individual-pore phase equilibrium to a two-dimensional pore network to study the impact of pore size distribution on the phase transition of hydrocarbon mixtures. Later, Song et al. [47] coupled an individual-pore phase equilibrium model that accounts for the impact of pore geometry to a static pore network model and also studied the relative permeability problem. More recently, Chen et al. [48] developed a new modeling framework that couples an individual-pore phase equilibrium model to a dynamic pore network model and investigated the impact of phase change on two-phase displacement, though capillary pressure was not included in their phase-equilibrium formulation. In addition to the above pore-scale studies, the individual-pore phase equilibrium model has also been employed in continuum-scale models to study the impact of pore size distribution on the phase behavior, e.g., the suppression of bubble point pressure [49,50]. These studies examined the phase behavior in a heterogeneous computational domain consisting of 2 or 3 homogeneous regions by applying an individual-pore phase equilibrium model to each region.

Accounting for the pressure differential alone (i.e., without accounting for fluid-wall interactions) in the phase equilibrium model cannot predict the deviation of the critical point (i.e., critical pressure and temperature) under nanoconfinement—a phenomenon commonly observed in nanofluidic experiments and advanced theoretical simulations [51–56]. To address this limitation, several studies have introduced an additional phase in the affinity of the solid surface (i.e., an adsorbed phase in addition to the bulk phases of liquid and vapor) to account for the fluid-wall interactions [57–59]. Travalloni et al. [57,58] developed a sophisticated thermodynamic phase equilibrium model for the adsorbed phase and the bulk phases. Their model was able to predict different types of adsorption isotherms and different multiphase configurations under nanoconfinement. Using a more practical approach, Sandoval et al. [59] developed a model that couples the multicomponent Langmuir (ML) isotherm (for the adsorbed phase) to an individual-pore phase equilibrium model. Their model successfully predicted the shifted phase behavior (for both the phase envelope and critical point) due to nanoconfinement effects.

The work of Sandoval et al. [59] provides a promising practical approach to represent the nanoconfined phase behaviors in a phase equilibrium model. But the current formulation only applies to a single tube-type pore with a circular cross-section. Other pore geometries that may better represent the realistic pore structures, such as tubes with square or triangular cross-sections, are yet to be accounted for. More importantly, the single-pore formulation needs to be rigorously upscaled to fully represent the complex multiscale pore-network structures in shale rocks. Our objective was to address these two critical issues and develop an upscaling framework that can represent the nanoconfined phase behaviors in complex nanopore networks. Specifically, (1) we first generalize the individual-pore phase equilibrium model of Sandoval et al. [59] to account for different pore geometries, and (2) then couple the generalized model to a complex pore network to develop a new upscaling framework for deriving macroscopic phase behavior formulations at the network-scale. Employing the generalized individual-pore phase equilibrium model to each pore and assuming thermodynamic equilibrium across the pore network allow us to derive the macroscopic phase behavior variables for the entire network. The end result is a network-scale phase equilibrium model that naturally accounts for the nanoconfinement effects in a complex pore network with pores varying in size and geometry. To the best of our knowledge, this is the first upscaling framework that allows one to derive the macroscopic phase behavior in pore networks that are representative of the realistic pore structures of shale rocks.

The paper is organized as follows. We present the mathematical formulations and the numerical algorithms for both the generalized individual-pore phase equilibrium model and the network-scale phase equilibrium model in Section 2. In Section 3, we employ the newly derived individual-pore and network-scale phase equilibrium models to analyze the impact of capillary pressure, competitive adsorption, pore size, geometry, and the multiscale pore structures on the phase behaviors under nanoconfinement. This is followed by discussions of the key ingredients of the upscaling framework and its implications to reservoir simulations for liquid-rich shale formations in Section 4. We close with concluding remarks in Section 5.

2. Method

We present the mathematical formulations and the numerical algorithms for: (1) the generalized individual-pore phase equilibrium model in Section 2.1, and (2) the network-scale phase equilibrium model in Section 2.2.

2.1. Phase equilibrium model in a single nanopore

We generalize the individual-pore phase equilibrium model of Sandoval et al. [59]—derived for a pore with a circular cross-section—to allow for pores with more general geometries including tubes with square and triangular cross-sections. The different geometries allow for representing more realistic pore structures of rocks, e.g., they can more accurately replicate different shape factors and surface areas of a pore [60].

2.1.1. Thermodynamic equilibrium

Inside a nanopore, a hydrocarbon mixture may exist in three different phases, i.e., liquid, vapor, or adsorbed phase (see Fig. 1). When two or three phases coexist, we assume thermodynamic equilibrium among them, i.e., the fugacity of any component is equal in the liquid (l), vapor (v), and adsorbed (ad) phases,

$$f^{k,\mathrm{l}} = f^{k,\mathrm{v}} = f^{k,\mathrm{ad}}, \tag{1}$$

where $f^{k,\alpha}$ is the fugacity of component k ($k = 1, 2, 3, \ldots, N_c$, where N_c is the total number of components) in the α phase ($\alpha =$ "l", "v", or "ad"), which is a function of the temperature T, pressure p^{α}, and composition of the α phase [61, ch. 4&6]. Let x^k, y^k, and w^k denote the mole fraction of component k in the liquid, vapor, and adsorbed phases, respectively, $\mathbf{x} = \{x^k\}$, $\mathbf{y} = \{y^k\}$, and $\mathbf{w} = \{w^k\}$ ($k = 1, 2, 3, \ldots, N_c$) would then represent the composition of the liquid, vapor, and adsorbed phases. $f^{k,\alpha}$ has the following forms

$$\begin{aligned} &f^{k,\mathrm{l}} = x^k p^{\mathrm{l}} \varphi^{k,\mathrm{l}}(T, p^{\mathrm{l}}, \mathbf{x}),\ f^{k,\mathrm{v}} = y^k p^{\mathrm{v}} \varphi^{k,\mathrm{v}}(T, p^{\mathrm{v}}, \mathbf{y}), \\ &f^{k,\mathrm{ad}} = w^k p^{\mathrm{ad}} \varphi^{k,\mathrm{ad}}(T, p^{\mathrm{ad}}, \mathbf{w}), \end{aligned} \tag{2}$$

where $\varphi^{k,\alpha}$ is the fugacity coefficient of component k in the α phase, which is a function of the temperature, pressure, and composition of the α phase [61, ch. 4].

Using ψ^{α} to denote the mole fraction of the α phase, the mass conservation of component k in the three phases can be written as

$$\psi^{\mathrm{l}} x^k + \psi^{\mathrm{v}} y^k + \psi^{\mathrm{ad}} w^k = z^{k,\mathrm{f}}, \tag{3}$$

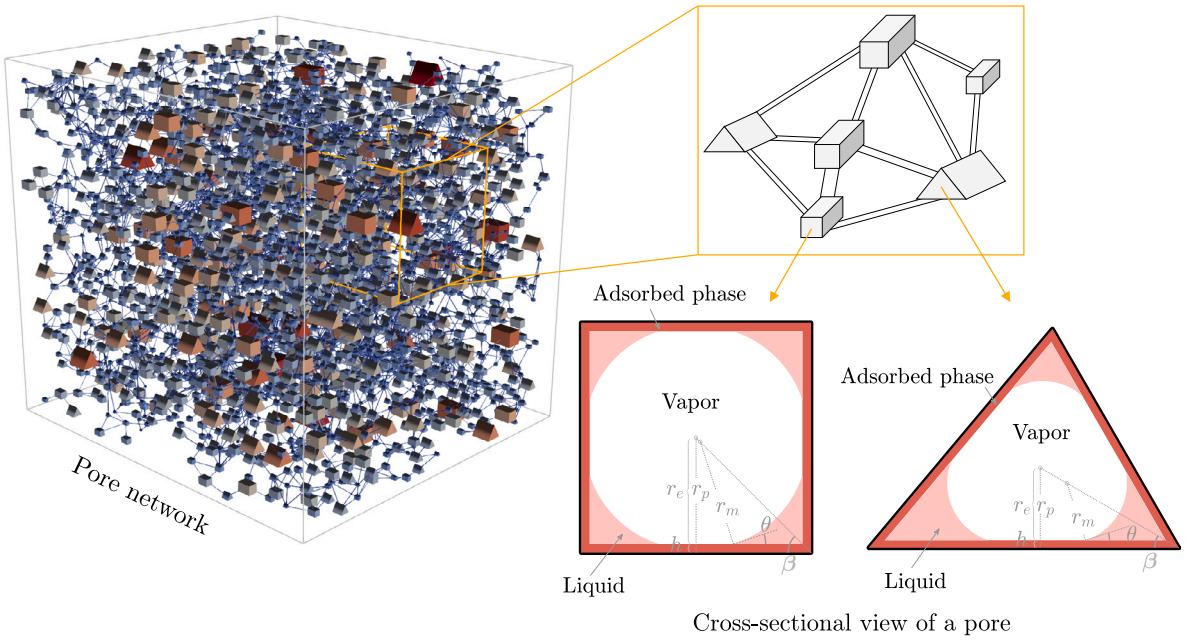

Fig. 1. Schematic of a pore network consisting of pores with square or triangular cross-sections and the cross-sectional view of a pore in the presence of liquid, vapor, and adsorbed phases.

where $z^{k,\mathrm{f}}$ is the mole fraction of component k in the total feed (the superscript "f" refers to "feed"). By definition, the mole fractions of all three phases sum to unity

$$\psi^{\mathrm{l}} + \psi^{\mathrm{v}} + \psi^{\mathrm{ad}} = 1. \tag{4}$$

Similarly, the summation of the mole fractions for all N_c components in each phase is equal to unity, i.e.,

$$\sum_{k=1}^{N_c} x^k = \sum_{k=1}^{N_c} y^k = \sum_{k=1}^{N_c} w^k = 1. \tag{5}$$

When liquid and vapor coexist in a pore, they form fluid-fluid interfaces that lead to a pressure difference between the two fluids (i.e., capillary pressure). The capillary pressure needs to be accounted for when computing the fugacities in the vapor and liquid phases (Eq. (2)). Assuming vapor is the nonwetting phase and liquid is the wetting phase, the capillary pressure p^c is defined as

$$p^{\mathrm{v}} - p^{\mathrm{l}} = p^c. \tag{6}$$

The mathematical formulation for p^c will be presented in the following Section 2.1.2.

2.1.2. Capillary pressure

p^c may be described by the Young–Laplace equation,

$$p^c = \sigma\left(\frac{1}{r_{m,1}} + \frac{1}{r_{m,2}}\right). \tag{7}$$

σ is the interfacial tension between liquid and vapor, which can be computed by $\sigma^{1/4} = \sum_{k=1}^{N_c} \chi^k \left(x^k \rho^{\mathrm{l}} - y^k \rho^{\mathrm{v}}\right)$, where χ^k is the parachor of pure component k [61, ch. 4]. $r_{m,1}$ and $r_{m,2}$ are the two principal radii of curvature of the fluid-fluid interface. For a pore with a circular cross-section, $r_{m,1} = r_{m,2}$ and they are independent of the phase saturation. For a pore with a square or triangular cross-section, the radius of curvature along the pore length is infinite (see Fig. 1). Thus, only the principal radius of curvature in the cross-sectional plane is used to compute p^c. The principal radius of curvature in the cross-sectional plane is a function of phase saturation, which will be presented in the following.

To simplify the notation, we drop the number in the subscript and simply use r_m to denote the principal radius of curvature in the cross-sectional plane here and in the rest of the paper. As shown in Fig. 1, before the interfaces meet (i.e., $s^{\mathrm{l}} \le s^{\mathrm{l}}_c$, where s^{l} is the liquid saturation in the bulk phases and s^{l}_c is the s^{l} when the interfaces meet), r_m is an explicit expression of the cross-section geometry, contact angle θ, and liquid saturation in the bulk phases s^{l} (see Eq. (8)). After the interfaces meet (i.e., $s^{\mathrm{l}} > s^{\mathrm{l}}_c$), the curvature and the formulation of r_m become more complicated. Different forms of r_m (including a nonmonotonic r_m-s^{l} function, a monotonic r_m-s^{l} function, and a constant r_m) have been proposed for $s^{\mathrm{l}} > s^{\mathrm{l}}_c$ in the literature [48,62–64]. Here, we assume r_m is constant for $s^{\mathrm{l}} > s^{\mathrm{l}}_c$ and is equal to the r_m corresponding to $s^{\mathrm{l}} = s^{\mathrm{l}}_c$ [48]. Since the fluid-fluid interface may not be defined when the radius of curvature becomes small, e.g., on the order of nanometers, we assume the radius of the curvature has a minimum value r_0. Namely, r_m does not decrease with s^{l} when $s^{\mathrm{l}} \le s^{\mathrm{l}}_0$, where s^{l}_0 is the liquid saturation in the bulk phases corresponding to $r_m = r_0$.

To derive the general expression for r_m, we define the following four geometrical parameters to represent the fluid distribution in the cross-sectional plane of a pore: (1) $\tilde{a}_e$, the area occupied by the bulk phases when $r_e = 1$, where r_e is the effective pore radius (i.e., the radius of the inscribed circle of the area available for the bulk phases as shown in Fig. 1); $\tilde{a}_e = \sum_{j=1}^{N_\beta} \cot\beta_j$, where β is the half corner angle and N_β is the number of corners in the cross-section of a pore. (2) $\tilde{a}_m$, the area occupied by the liquid phase when $r_m = 1$; $\tilde{a}_m = \sum_{j=1}^{N_\beta} \cos\theta\cos(\theta + \beta_j)/\sin\beta_j - (\pi/2 - \theta - \beta_j)$. (3) $\tilde{\ell}_e$, the perimeter of the area occupied by the bulk phases when $r_e = 1$; $\tilde{\ell}_e = \sum_{j=1}^{N_\beta} 2\cot\beta_j$. (4) $\tilde{\ell}_m$, the total length of the interfaces between the liquid and the adsorbed phases when $r_m = 1$; $\tilde{\ell}_m = \sum_{j=1}^{N_\beta} 2\cos(\theta + \beta_j)/\sin\beta_j$. Using the above four geometric parameters, s^{l}_0 and s^{l}_c can be expressed as $s^{\mathrm{l}}_0 = (r_0^2\tilde{a}_m)/(r_e^2\tilde{a}_e)$ and $s^{\mathrm{l}}_c = (r^2_{m,c}\tilde{a}_m)/(r_e^2\tilde{a}_e)$, where $r_{m,c}$ is the r_m when interfaces meet, namely, $r_{m,c} = r_e\tilde{\ell}_e/\tilde{\ell}_m$. Then, r_m has the following form

$$r_m = \begin{cases} r_0 & 0 \le s^{\mathrm{l}} \le s^{\mathrm{l}}_0, \\ \left(s^{\mathrm{l}} r_e^2 \tilde{a}_e/\tilde{a}_m\right)^{1/2} & s^{\mathrm{l}}_0 < s^{\mathrm{l}} \le s^{\mathrm{l}}_c, \\ r_e\tilde{\ell}_e/\tilde{\ell}_m & s^{\mathrm{l}}_c < s^{\mathrm{l}} \le 1. \end{cases} \tag{8}$$

s^{l} can be computed via

$$s^{\mathrm{l}} = \frac{\gamma/\rho^{\mathrm{l}}}{1/\rho^b} = \frac{\gamma/\rho^{\mathrm{l}}}{\gamma/\rho^{\mathrm{l}} + (1-\gamma)/\rho^{\mathrm{v}}}, \tag{9}$$

where γ is the mole fraction of liquid in the bulk phases, i.e., $\gamma = \psi^{\mathrm{l}}/(\psi^{\mathrm{l}} + \psi^{\mathrm{v}})$. ρ^{b} is the bulk molar density (the superscript "b" refers to "bulk"). ρ^{l} and ρ^{v} are the molar densities of liquid and vapor phases, respectively, which are functions of temperature, pressure, and phase composition, and can be computed via the Peng-Robinson equation-of-state (EOS) [65,66].

2.1.3. Adsorption

In the adsorbed phase, the fugacity of a component, $f^{k,\mathrm{ad}}$, is a function of temperature T, pressure p^{ad}, and mole fraction of the component w^k (see Eqs. (2)). Using ξ^k to denote the amount (in mole) of component k in the adsorbed phase, w^k can be written as

$$w^k = \frac{\xi^k}{\sum_{j=1}^{N_c} \xi^j}. \tag{10}$$

Now, $f^{k,\mathrm{ad}}$ is a function of T, p^{ad}, and ξ^k. The functional form can be determined by using sophisticated adsorption models that explicitly represent the fluid-wall interactions (e.g., an extended version of the generalized van der Waals theory) [57,58] or via relatively simple adsorption models that employ an isotherm equation (e.g., an ML model) [59]. Here, we follow Sandoval et al. [59] and employ an ML model, i.e., Eq. (11), to provide the relationship among $f^{k,\mathrm{ad}}$, T, and ξ^k (note that because the ML model does not involve an EOS for the adsorbed phase, p^{ad} is not a model parameter).

$$\xi^k = \xi^{\max,k}(T)\frac{b^k(T) f^{k,\mathrm{ad}}}{1 + \sum_{j=1}^{N_c} b^j(T) f^{j,\mathrm{ad}}}, \tag{11}$$

where $\xi^{\max,k}$ is the maximum adsorption and b^k is the adsorption equilibrium constant. $\xi^{\max,k}$ and b^k can be determined for different rock materials by fitting the ML model to adsorption data obtained from batch experiments or generated from more advanced models such as the multicomponent potential theory of adsorption (MPTA) model [59,67]. Additionally, we can use the ξ^k given by Eq. (11) to compute the molar fraction of adsorbed phase ψ^{ad} as

$$\psi^{\mathrm{ad}} = \frac{\sum_{j=1}^{N_c} \xi^j}{\rho^{\mathrm{b}}(v - v^{\mathrm{ad}}) + \sum_{j=1}^{N_c} \xi^j}, \tag{12}$$

where v is the pore volume, and v^{ad} is the volume of the adsorbed phase in a pore. Here we assume: (1) the pore wall is homogeneous, (2) the adsorbed phase has a uniform density and a constant thickness, h [68], and (3) the adsorbed layer always exists, i.e., $\xi^{\max,k}$ and h are positive [59,69,70]. Therefore, v^{ad} for a pore with a circular cross-section is equal to $\pi\ell\left(r_p^2 - (r_p - h)^2\right)$ or $\pi\ell(r_p^2 - r_e^2)$, while v^{ad} for a pore with a square or triangular cross-section can be computed as

$$v^{\mathrm{ad}} = \sum_{j=1}^{N_\beta} 2\ell\left(h r_p \cot\beta_j - \frac{1}{2}h^2\cot\beta_j\right), \tag{13}$$

where r_p is the pore size (i.e., the radius of the inscribed circle of the cross-section of a pore) and ℓ is the pore length (i.e., the length of the tube) (see Fig. 1).

2.1.4. Numerical algorithm

Eqs. (1)–(13) represent a closed mathematical formulation for the phase equilibrium among liquid, vapor, and adsorbed phases in a single nanopore. For a hydrocarbon mixture, given the temperature T, pressure of one bulk phase (e.g., p^{v}), and composition in the total feed $z^{k,\mathrm{f}}$, our goal is to solve for the phase fractions (i.e., ψ^{l}, ψ^{v}, and ψ^{ad}) and the composition of each of the phases (i.e., $\mathbf{x}$, $\mathbf{y}$, and $\mathbf{w}$). After some rearrangement, we obtain

$$\begin{cases} x^k p^{\mathrm{l}}\varphi^{k,\mathrm{l}}(T, p^{\mathrm{l}}, \mathbf{x}) = y^k p^{\mathrm{v}}\varphi^{k,\mathrm{v}}(T, p^{\mathrm{v}}, \mathbf{y}), & \Leftrightarrow\ f^{k,\mathrm{l}} = f^{k,\mathrm{v}}, \\ \gamma x^k + (1-\gamma) y^k = (z^{k,\mathrm{f}} - \psi^{\mathrm{ad}} w^k)/(1 - \psi^{\mathrm{ad}}), \\ \sum_{k=1}^{N_c} x^k = \sum_{k=1}^{N_c} y^k = 1, \\ p^{\mathrm{v}} - p^{\mathrm{l}} = p^{\mathrm{c}}. \end{cases} \tag{14}$$

Now the primary unknown variables are γ, $\mathbf{x}$, and $\mathbf{y}$. We further manipulate Eqs. (14) by introducing two sets of new variables κ and $\mathbf{z}^{\mathrm{b}}$ (where $\kappa = \{\kappa^k\}$ and $\mathbf{z}^{\mathrm{b}} = \{z^{k,\mathrm{b}}\}$ with $k = 1, 2, 3, \ldots, N_c$) to replace $\mathbf{x}$ and $\mathbf{y}$ so that the primary variables become γ, κ, and $\mathbf{z}^{\mathrm{b}}$. κ^k is the equilibrium coefficient of component k, where $\kappa^k = y^k/x^k$. $z^{k,\mathrm{b}}$ is the mole fraction of component k in the bulk phases, which can be computed via

$$z^{k,\mathrm{b}} = \frac{z^{k,\mathrm{f}}\left[\rho^{\mathrm{b}}(v - v^{\mathrm{ad}}) + \sum_{j=1}^{N_c}\xi^j\right] - \xi^k}{\rho^{\mathrm{b}}(v - v^{\mathrm{ad}})}. \tag{15}$$

Once κ^k and $z^{k,\mathrm{b}}$ are known, x^k and y^k can be computed as

$$x^k = \frac{z^{k,\mathrm{b}}}{\gamma + (1-\gamma)\kappa^k},\ y^k = \frac{z^{k,\mathrm{b}}\kappa^k}{\gamma + (1-\gamma)\kappa^k}. \tag{16}$$

The primary variables γ, κ, and $\mathbf{z}^{\mathrm{b}}$ can be solved using a standard flash calculation with some modifications, i.e., we need to update the pressure of one of the bulk phases (i.e., p^{l} if p^{v} is given, and vice versa) and the composition in the bulk phases (i.e., $\mathbf{z}^{\mathrm{b}}$) during the iterations. We summarize the algorithmic steps below.

1. Set the initial guesses of the liquid pressure and composition in the bulk phases as $p^{\mathrm{l}} = p^{\mathrm{v}}$ and $\mathbf{z}^{\mathrm{b}} = \mathbf{z}^{\mathrm{f}}$, respectively.

2. Compute the initial guess of the equilibrium coefficients κ via the Wilson's equation,

$$\kappa^k = \frac{p_c^k}{p^{\mathrm{v}}}\exp\left[5.373\left(1+\omega^k\right)\left(1 - \frac{T_c^k}{T}\right)\right], \tag{17}$$

where p_c^k and T_c^k are the critical pressure and critical temperature of component k, respectively. ω^k is the acentric factor of component k.

3. Update the mole fraction of liquid in the bulk phases γ via solving the Rachford-Rice equation (which is equivalent to the third equation in Eqs. (14)),

$$\sum_{k=1}^{N_c}\frac{\left(\kappa^k - 1\right) z^{k,\mathrm{b}}}{\gamma + (1-\gamma)\kappa^k} = 0. \tag{18}$$

4. Update the following variables: the composition in each of the bulk phases $\mathbf{x}$ and $\mathbf{y}$ via Eqs. (16), the liquid saturation in the bulk phases s^{l} via Eq. (9), the liquid phase pressure p^{l} via Eq. (6), the fugacity in each of the bulk phases $f^{k,\mathrm{l}}$ and $f^{k,\mathrm{v}}$ for all N_c components according to the first equation in Eqs. (14), and the amount of component k in the adsorbed phase ξ^k for all N_c components via Eq. (11).

5. Update the compositions in the bulk phases $\mathbf{z}^{\mathrm{b}}$ via Eq. (15).

6. Update the equilibrium coefficients κ via

$$\kappa^k = \frac{p^{\mathrm{l}}\cdot\varphi^{k,\mathrm{l}}(T, p^{\mathrm{l}}, \mathbf{x})}{p^{\mathrm{v}}\cdot\varphi^{k,\mathrm{v}}(T, p^{\mathrm{v}}, \mathbf{y})}. \tag{19}$$

7. Repeat steps $3 \sim 6$ till $f^{k,\mathrm{l}} = f^{k,\mathrm{v}}$ is satisfied for all N_c components (i.e., $\sum_{k=1}^{N_c}\|1 - f^{k,\mathrm{l}}/f^{k,\mathrm{v}}\|^2 < \epsilon$, where ϵ is a small positive number).

2.2. Upscaled phase equilibrium model for realistic pore networks

We upscale the generalized individual-pore phase equilibrium model presented in Section 2.1 to describe the nanoconfined phase behaviors in complex nanopore networks in shale rocks. The generalized individual-pore phase equilibrium model (Section 2.1) is employed to each pore of a pore network. The pores are represented by tubes with square and triangular cross-sections to better represent realistic pores with a wide range of shape factors [60]. Then by assuming thermodynamic equilibrium across the pore network, we integrate the phase behavior variables for all individual pores to derive macroscopic phase behavior variables for the entire pore network. The macroscopic phase behavior variables are then used to formulate a network-scale phase equilibrium model. Below, we present the upscaled phase equilibrium formulations and the numerical algorithm to solve the macroscopic phase behavior variables.

2.2.1. Thermodynamic equilibrium in a pore network

To derive an upscaled phase equilibrium model for a nanopore network that consists of N_p pores, we assume thermodynamic equilibrium, i.e., chemical and mechanical equilibrium, across the entire pore network. The chemical equilibrium leads to equal fugacity for component k in each phase in all of the N_p pores,

$$\begin{cases} f_1^{k,\mathrm{l}} = f_2^{k,\mathrm{l}} = \cdots = f_{N_p}^{k,\mathrm{l}} = F^{k,\mathrm{l}}, \\ f_1^{k,\mathrm{v}} = f_2^{k,\mathrm{v}} = \cdots = f_{N_p}^{k,\mathrm{v}} = F^{k,\mathrm{v}}, \\ f_1^{k,\mathrm{ad}} = f_2^{k,\mathrm{ad}} = \cdots = f_{N_p}^{k,\mathrm{ad}} = F^{k,\mathrm{ad}}, \end{cases} \tag{20}$$

where $F^{\alpha,k}$ is the uniform fugacity of component k in the α phase, which we refer to as the macroscopic fugacities of the pore network.

The mechanical equilibrium leads to equal pressure in each phase for all pores,

$$\begin{cases} p_1^{\mathrm{l}} = p_2^{\mathrm{l}} = \cdots = p_{N_p}^{\mathrm{l}} = P^{\mathrm{l}}, \\ p_1^{\mathrm{v}} = p_2^{\mathrm{v}} = \cdots = p_{N_p}^{\mathrm{v}} = P^{\mathrm{v}}, \\ p_1^{\mathrm{ad}} = p_2^{\mathrm{ad}} = \cdots = p_{N_p}^{\mathrm{ad}} = P^{\mathrm{ad}}, \end{cases} \tag{21}$$

where P^{l}, P^{v}, and P^{ad} are the uniform liquid, vapor, and adsorbed phase pressures, which we refer to as the macroscopic liquid, vapor, and adsorbed phase pressures of the pore network, respectively. Similarly, the mole fraction of each component k is equal in each phase, which yields

$$\begin{cases} x_1^k = x_2^k = \cdots = x_{N_p}^k = X^k, \\ y_1^k = y_2^k = \cdots = y_{N_p}^k = Y^k, \\ w_1^k = w_2^k = \cdots = w_{N_p}^k = W^k, \end{cases} \tag{22}$$

where X^k, Y^k, and W^k are the macroscopic mole fraction of component k in the liquid, vapor, and adsorbed phases of the pore network, respectively. The density of each phase is also equal for all pores

$$\begin{cases} \rho_1^{\mathrm{l}} = \rho_2^{\mathrm{l}} = \cdots = \rho_{N_p}^{\mathrm{l}} = \rho^{\mathrm{l}}, \\ \rho_1^{\mathrm{v}} = \rho_2^{\mathrm{v}} = \cdots = \rho_{N_p}^{\mathrm{v}} = \rho^{\mathrm{v}}, \\ \rho_1^{\mathrm{ad}} = \rho_2^{\mathrm{ad}} = \cdots = \rho_{N_p}^{\mathrm{ad}} = \rho^{\mathrm{ad}}, \end{cases} \tag{23}$$

where ρ^{l}, ρ^{v}, and ρ^{ad} are the macroscopic liquid, vapor, and adsorbed phase densities in the pore network, respectively. Similarly, we define the macroscopic interfacial tension between liquid and vapor phases as σ, which represents the uniform interfacial tension for all pores.

In addition to the above macroscopic variables, we define the following additional macroscopic variables: (1) Ψ^{α}, the mole fraction of the α phase in the pore network; (2) $\mathbf{Z}^{\mathrm{f}}$, defined as $\mathbf{Z}^{\mathrm{f}} = \{Z^{k,\mathrm{f}}\}$ with $k = 1, 2, 3, \ldots, N_c$, where $Z^{k,\mathrm{f}}$ the mole fraction of component k in the total feed of the pore network. We then use the macroscopic variables to formulate the network-scale phase equilibrium model, which has the same form as the individual-pore phase equilibrium model (Section 2.1). The thermodynamic equilibrium among liquid, vapor, and adsorbed phase yields

$$F^{k,\mathrm{l}} = F^{k,\mathrm{v}} = F^{k,\mathrm{ad}}. \tag{24}$$

The fugacities $F^{k,\mathrm{l}}$, $F^{k,\mathrm{v}}$, and $F^{k,\mathrm{ad}}$ have the following forms

$$\begin{aligned} &F^{k,\mathrm{l}} = X^k P^{\mathrm{l}} \Phi^{k,\mathrm{l}}(T, P^{\mathrm{l}}, \mathbf{X}),\ F^{k,\mathrm{v}} = Y^k P^{\mathrm{v}} \Phi^{k,\mathrm{v}}(T, P^{\mathrm{v}}, \mathbf{Y}), \\ &F^{k,\mathrm{ad}} = W^k P^{\mathrm{v}} \Phi^{k,\mathrm{ad}}(T, P^{\mathrm{ad}}, \mathbf{W}), \end{aligned} \tag{25}$$

where $\mathbf{X} = \{X^k\}$, $\mathbf{Y} = \{Y^k\}$, and $\mathbf{W} = \{W^k\}$ $(k = 1, 2, 3, \ldots, N_c)$ denote the composition in the liquid, vapor, and adsorbed phase of the network, respectively; and $\Phi^{k,\alpha}$ is the fugacity coefficient of component k in the α phase, which is a function of the temperature, pressure, and composition in the α phase [61, ch. 4]. The mass conservation of component k in the three phases can be written as

$$\Psi^{\mathrm{l}} X^k + \Psi^{\mathrm{v}} Y^k + \Psi^{\mathrm{ad}} W^k = Z^{k,\mathrm{f}}. \tag{26}$$

The macroscopic mole fractions of all three phases sum to unity

$$\Psi^{\mathrm{l}} + \Psi^{\mathrm{v}} + \Psi^{\mathrm{ad}} = 1. \tag{27}$$

Additionally, the summation of the macroscopic mole fractions for all N_c components in each phase is equal to unity, i.e.,

$$\sum_{k=1}^{N_c} X^k = \sum_{k=1}^{N_c} Y^k = \sum_{k=1}^{N_c} W^k = 1. \tag{28}$$

Similar to the single nanopore formulations, when liquid and vapor coexist in a pore network, the capillary pressure needs to be accounted for when computing the fugacities. Because the pressures in each phase are uniform across the pore network, the capillary pressures are also uniform. The uniform capillary pressure P^c (which we refer to as the macroscopic capillary pressure) is defined as

$$P^{\mathrm{v}} - P^{\mathrm{l}} = P^c. \tag{29}$$

The mathematical formulation for P^c will be presented in the following Section 2.2.2.

2.2.2. Capillary pressure

The uniform capillary pressure (P^c) leads to a uniform principle radius of curvature of the liquid-vapor interfaces in the cross-sectional plane in all pores (note that because pores are represented by tubes with square and triangular cross-sections, the principle radius of curvature along the pore length is infinite). We use R_m to denote the uniform principle radius of curvature, which is referred to as the macroscopic principle radius of curvature of the pore network. R_m is a function of the pore size distribution and the macroscopic liquid phase saturation $S^{\mathrm{l}} = \sum_{i=1}^{N_p} s_i^{\mathrm{l}}(v_i - v_i^{\mathrm{ad}})/(V - V^{\mathrm{ad}})$, where $V = \sum_{i=1}^{N_p} v_i$ is the total pore volume of the pore network, s_i^{l} is the liquid saturation in pore i (see Appendix A.1 for the detailed $S^{\mathrm{l}} - s_i^{\mathrm{l}}$ expression), and $V^{\mathrm{ad}} = \sum_{i=1}^{N_p} v_i^{\mathrm{ad}}$ is the total volume of the adsorbed phase in the pore network. We derive the expression for R_m as follows.

When $S^{\mathrm{l}} \le S_0^{\mathrm{l}}$ ($S_0^{\mathrm{l}} = \sum_{i=1}^{N_p} s_{0,i}^{\mathrm{l}}(v_i - v_i^{\mathrm{ad}})/(V - V^{\mathrm{ad}})$), $R_m = r_0$. As S^{l} increases from $S_{c,0}^{\mathrm{l}}$, smaller pores will gradually become saturated by liquid. Without of loss of generality, suppose that the pores are numbered such that $r_{p,i-1} \le r_{p,i}$ for $1 \le i \le N_p$. If several pores have the same size, they are numbered next to each other. When pore i is the smallest unsaturated pore (if several pores share the same size, i refers to the number for the first pore), R_m increases with S^{l} before the liquid-vapor interfaces meet in pore i (i.e., $s_i^{\mathrm{l}} < s_{c,i}^{\mathrm{l}}$). Then, after the liquid-vapor interfaces meet in pore i (i.e., $s_{c,i}^{\mathrm{l}} \le s_i^{\mathrm{l}} < 1$), R_m becomes constant and $R_m = r_{m,i} = r_{e,i}\tilde{\ell}_{e,i}/\tilde{\ell}_{m,i}$ (see Eq. (8)). Once pore i becomes saturated, R_m will continue to increase with S^{l} following the same procedure outlined above until all of the pores become saturated by the liquid phase. A detailed illustration of the above procedures is presented in Fig. A.1. Let $S_{c,i}^{\mathrm{l}}$ be the S^{l} corresponding to $s_i^{\mathrm{l}} = s_{c,i}^{\mathrm{l}}$ and $S_{s,i}^{\mathrm{l}}$ be the S^{l} corresponding to $s_i^{\mathrm{l}} \to 1$ (i.e., pore i becomes saturated by the liquid), R_m for $S^{\mathrm{l}} > S_0^{\mathrm{l}}$ can be computed as

$$R_m = \begin{cases} \left(\dfrac{S^{\mathrm{l}}(V - V^{\mathrm{ad}}) - \sum_{j=1}^{i-1}(v_j - v_j^{\mathrm{ad}})}{\sum_{j=i}^{N_p} \ell_j \tilde{a}_{m,j}} \right)^{1/2} & S_{s,i-1}^{\mathrm{l}} < S^{\mathrm{l}} \le S_{c,i}^{\mathrm{l}}, \\ r_{e,i}\tilde{\ell}_{e,i}/\tilde{\ell}_{m,i} & S_{c,i}^{\mathrm{l}} < S^{\mathrm{l}} \le S_{s,i}^{\mathrm{l}}. \end{cases} \tag{30}$$

The macroscopic liquid phase saturation S^{l} can be computed by

$$S^{\mathrm{l}} = \frac{\Gamma/\rho^{\mathrm{l}}}{1/\rho^{\mathrm{b}}} = \frac{\Gamma/\rho^{\mathrm{l}}}{\Gamma/\rho^{\mathrm{l}} + (1 - \Gamma)/\rho^{\mathrm{v}}}, \tag{31}$$

where Γ is the macroscopic mole fraction of liquid phase in the bulk phases of the pore network, i.e., $\Gamma = \Psi^{\mathrm{l}}/(\Psi^{\mathrm{l}} + \Psi^{\mathrm{v}})$. ρ^b is the molar density of the bulk phases in the entire network. After the macroscopic

principle radius of curvature R_m is computed, the macroscopic capillary pressure P^c in Eq. (29) can be obtained via

$$P^c = \frac{\sigma}{R_m}. \tag{32}$$

2.2.3. Adsorption

In the adsorbed phase, the macroscopic fugacity of a component, $F^{k,\mathrm{ad}}$, is a function of temperature T, pressure P^{ad}, and mole fraction of the component W^k (see Eqs. (25)). Using Ξ^k to denote the total amount (in mole) of component k in the adsorbed phase of the network, W^k can be written as

$$W^k = \frac{\Xi^k}{\sum_{j=1}^{N_c} \Xi^j}. \tag{33}$$

Therefore, $F^{k,\mathrm{ad}}$ is a function of T, P^{ad}, and Ξ^k. Similar to the individual-pore model (Section 2.1.3), we can link $F^{k,\mathrm{ad}}$, T, and Ξ^k by applying the ML model to each pore. Ξ^k is the sum of ξ_i^k across the entire network (see Eq. (11))

$$\Xi^k = \sum_{i=1}^{N_p} \xi_i^k = \sum_{i=1}^{N_p} \xi_i^{\max,k}(T) \frac{b_i^k(T) F^{k,\mathrm{ad}}}{1 + \sum_{j=1}^{N_c} b_i^j(T) F^{j,\mathrm{ad}}}. \tag{34}$$

Similarly, the mole fraction of the adsorbed phase of the network Ψ^{ad} can be computed as

$$\Psi^{\mathrm{ad}} = \frac{\sum_{j=1}^{N_c} \Xi^{j,\mathrm{abs}}}{\rho^{\mathrm{b}}(V - V^{\mathrm{ad}}) + \sum_{j=1}^{N_c} \Xi^{j,\mathrm{abs}}}, \tag{35}$$

2.2.4. Numerical algorithm

Eqs. (24)–(35) represent a closed mathematical formulation for the network-scale phase equilibrium model. Given the temperature T, pressure of one bulk phase (e.g., P^{v}), and composition in the total feed $\mathbf{Z}^{\mathrm{f}}$ in a pore network, our goal is to solve for the mole fraction of each phase (i.e., Ψ^{ad}, Ψ^{l}, Ψ^{v}) and the composition in each phase (i.e., $\mathbf{X}$, $\mathbf{Y}$, and $\mathbf{W}$). Similar to the rearrangement done for the individual-pore formulations in Section 2.1.4, Eqs. (24)–(35) can be simplified as

$$\begin{cases} X^k P^{\mathrm{l}} \Phi^{k,\mathrm{l}}(T, P^{\mathrm{l}}, \mathbf{X}) = Y^k P^{\mathrm{v}} \Phi^{k,\mathrm{v}}(T, P^{\mathrm{v}}, \mathbf{Y}), & \Leftrightarrow \ F^{k,\mathrm{l}} = F^{k,\mathrm{v}}, \\ \Gamma X^k + (1-\Gamma) Y^k = (Z^{k,\mathrm{f}} - \Psi^{\mathrm{ad}} W^k)/(1-\Psi^{\mathrm{ad}}), & \\ \sum_{k=1}^{N_c} X^k = \sum_{k=1}^{N_c} Y^k = 1, & \\ P^{\mathrm{v}} - P^{\mathrm{l}} = P^{\mathrm{c}}. & \end{cases} \tag{36}$$

Similar to Section 2.1.4, we further manipulate Eqs. (36) by introducing two sets of new variables $\mathbf{K}$ and $\mathbf{Z}^{\mathrm{b}}$ (where $\mathbf{K} = \{\mathcal{K}^k\}$ and $\mathbf{Z}^{\mathrm{b}} = \{Z^{k,\mathrm{b}}\}$ with $k = 1, 2, 3, \ldots, N_c$) to replace $\mathbf{X}$ and $\mathbf{Y}$, so that the primary variables become Γ, $\mathbf{K}$, and $\mathbf{Z}^{\mathrm{b}}$. $\mathcal{K}^k$ is the macroscopic equilibrium coefficients, where $\mathcal{K}^k = Y^k/X^k$. $Z^{k,\mathrm{b}}$ is the macroscopic mole fraction of component k in the bulk phases, which can be computed via

$$Z^{\mathrm{b},k} = \frac{Z^{k,\mathrm{f}}\left(\rho^{\mathrm{b}}(V - V^{\mathrm{ad}}) + \sum_{j=1}^{N_c} \Xi^j\right) - \Xi^k}{\rho^{\mathrm{b}}(V - V^{\mathrm{ad}})}, \tag{37}$$

Once $\mathbf{K}$ and $\mathbf{Z}^{\mathrm{b}}$ are known, X^k and Y^k can be computed as

$$X^k = \frac{Z^{k,\mathrm{b}}}{\Gamma + (1-\Gamma)\mathcal{K}^k}, \ Y^k = \frac{Z^{k,\mathrm{b}} \mathcal{K}^k}{\Gamma + (1-\Gamma)\mathcal{K}^k}. \tag{38}$$

The primary variables Γ, $\mathbf{K}$, and $\mathbf{Z}^{\mathrm{b}}$ can be solved using a flash calculation identical to that of the individual-pore phase equilibrium model in Section 2.1.4. The only difference is that here all variables are macroscopic variables. Below, we summarize the algorithmic steps.

1. Set the initial guesses of the liquid pressure and the compositions in the bulk phases as $P^{\mathrm{l}} = P^{\mathrm{v}}$ and $\mathbf{Z}^{\mathrm{b}} = \mathbf{Z}^{\mathrm{f}}$, respectively.

2. Compute the initial guess of the macroscopic equilibrium coefficients $\mathbf{K}$ via the Wilson's equation,

$$\mathcal{K}^k = \frac{p_c^k}{P^{\mathrm{v}}} \exp\left[5.373\left(1+\omega^k\right)\left(1 - \frac{T_c^k}{T}\right)\right], \tag{39}$$

3. Update the macroscopic mole fraction of liquid in the bulk phases Γ via solving the Rachford-Rice equation (which is equivalent to the third equation in Eqs. (36)),

$$\sum_{k=1}^{N_c} \frac{\left(\mathcal{K}^k - 1\right) Z^{\mathrm{b},k}}{\Gamma + (1-\Gamma)\mathcal{K}^k} = 0. \tag{40}$$

4. Update the following variables: the macroscopic composition in each of the bulk phases $\mathbf{X}$ and $\mathbf{Y}$ via Eqs. (38), the macroscopic liquid saturation in the bulk phases S^{l} via Eq. (31), the macroscopic liquid phase pressure P^{l} via Eq. (29), the macroscopic fugacity in each of the bulk phases $F^{k,\mathrm{l}}$ and $F^{k,\mathrm{v}}$ according to the first equation in Eq. (36), and the total amount of component k in the adsorbed phase Ξ^k via Eqs. (34).

5. Update the macroscopic composition in the bulk phases $\mathbf{Z}^{\mathrm{b}}$ via Eq. (37).

6. Update the macroscopic equilibrium coefficients $\mathbf{K}$ via Eq. (41),

$$\mathcal{K}^k = \frac{P^{\mathrm{l}} \cdot \Phi^{k,\mathrm{l}}(T, P^{\mathrm{l}}, \mathbf{X})}{P^{\mathrm{v}} \cdot \Phi^{k,\mathrm{v}}(T, P^{\mathrm{v}}, \mathbf{Y})}, \tag{41}$$

7. Repeat steps 3 $\sim$ 6 till $F^{k,\mathrm{l}} = F^{k,\mathrm{v}}$ is satisfied for all N_c components (i.e., $\sum_{k=1}^{N_c} \|1 - F^{k,\mathrm{l}}/F^{k,\mathrm{v}}\|^2 < \epsilon$, where ϵ is a small positive number).

3. Results and analysis

We conduct three sets of simulations to demonstrate the applicability of the phase equilibrium models presented in Section 2. The first set of simulations employs the individual-pore phase equilibrium model to study the phase behavior of hydrocarbons in a single nanopore with different sizes and geometries. These single-pore simulations allow us to examine the impact of several factors on the nanoconfined phase behavior in a single nanopore, including capillary pressure, adsorption, pore size, and pore geometry (i.e., the geometry of the pore cross-section). The other two sets of simulations employ the network-scale phase equilibrium model to study the phase behavior in pore networks. Three pore networks (i.e., one two-scale pore network and two multiscale pore networks) are used as examples. These network-scale simulations allow us to investigate how the nanoconfined phase behavior of hydrocarbons manifests in complex pore structures that consist of pores spanning a wide range of sizes. For all of the simulations, we set the minimum radius of curvature (r_0) to 5 nm [14,27,59,71,72], the adsorption thickness (h) to 0.5 nm [59], and the contact angle (θ) to 0 unless stated elsewhere.

3.1. Phase behavior in a single nanopore

First of all, we compare our individual-pore phase equilibrium model to that of Sandoval et al. [59] for a pore with a circular cross-section (r_p = 10 nm) to verify our implementation. Comparisons of the phase envelopes are presented in Fig. A.2 in Appendix A.2. Two hydrocarbon mixtures are simulated including a binary mixture (C1 : C2 = 0.5 : 0.5) and a ternary mixture (C1 : C4 : C10 = 0.42 : 0.33 : 0.25). The thermodynamic properties of C1, C2, C4, and C10 including the critical pressure p^{cr}, the critical volume V^{cr}, the critical temperature T^{cr}, the acentric factor ω, and the molar weight are obtained from Sandoval et al. [59] and Pedersen et al. [61]. The excellent agreement between our results and those from Sandoval et al. [59] (Fig. A.2) provides a verification for our implementation.

We then use the individual-pore phase equilibrium model to investigate the impact of capillary pressure, adsorption, pore size, and pore geometry on the nanoconfined phase behavior in a single nanopore. We consider pores with two different pore geometries (i.e., square tube and equilateral triangular tube) and sizes (i.e., r_p = 10 nm and 100 nm). A binary mixture (C1 : C4 = 0.5 : 0.5) and a ternary mixture (C1 : C4 : C10 = 0.42 : 0.33 : 0.25) are examined. The ratios are molar

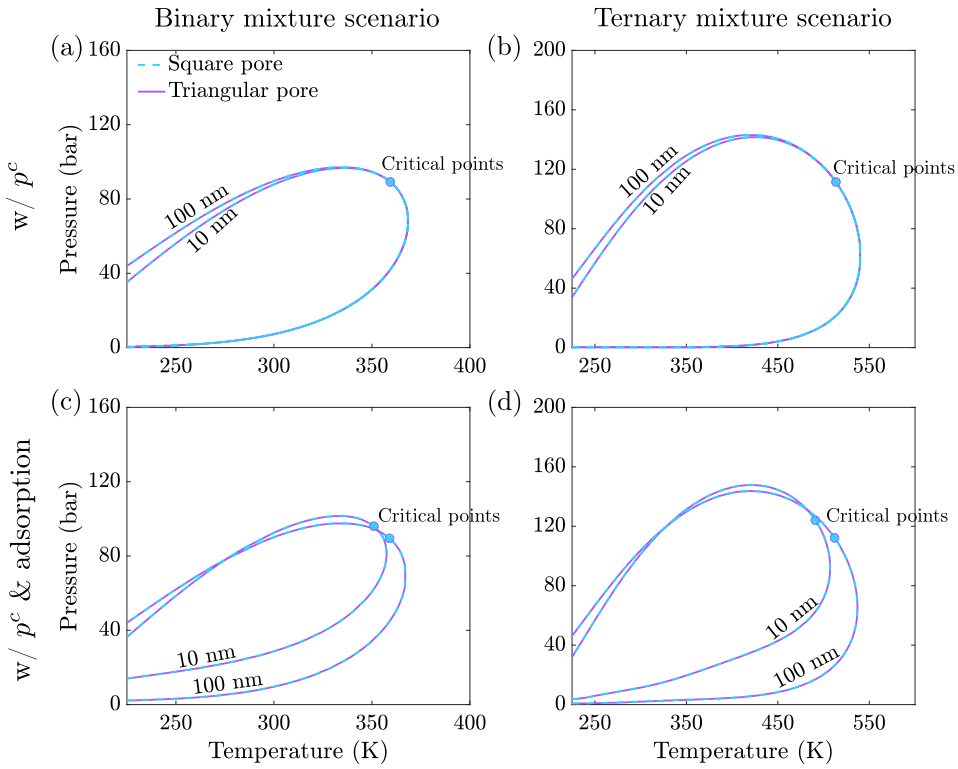

Fig. 2. Phase envelopes of a binary mixture (C1 : C4 = 0.5 : 0.5; left) and a ternary mixture (C1 : C4 : C10 = 0.42 : 0.33 : 0.25; right) in a single nanopore with different sizes (r_p = 10 nm and 100 nm) and geometries (tubes with square or triangular cross-sections). The results in row 1 (*a* and *b*) only include the capillary pressure, while those in row 2 (*c* and *d*) account for both capillary pressure and competitive adsorption. The critical points (i.e., critical pressure and temperature) for pores with a square cross-section are indicated by asterisks and those in pores with a triangular cross-section are indicated by circles.

ratios. These two mixtures will also be used for the other simulations presented in the rest of the paper.

For each mixture, we present the phase envelope (i.e., a line that surrounds the two-phase region on the *P-T* phase diagram) and the critical point (i.e., a point that separates the phase envelope into an upper branch, referred to as bubble point line, and a lower branch, referred to as dew point line). On the bubble point line, the mixture is in liquid phase. Thus, the liquid phase pressure is used as the reference pressure. Conversely, on the dew point line, the mixture is in vapor phase and the vapor phase pressure is used as the reference pressure.

When only capillary pressure (p^c) is included in the phase behavior model (Fig. 2a–b), the bubble point line shifts down as the pore size becomes smaller, while the dew point line remains unchanged. This is because $p^c = \sigma/r_m$, and $r_m = r_e$ on the bubble point line that decreases for a smaller pore, while $r_m = r_0$ on the dew point line that is independent of pore size (see Eqs. (7)–(8)). This is also the reason that the phase envelopes for the square and triangular cross-sections are identical—as long as the pore size is kept the same, r_e and r_0 do not change with the geometry of the cross-section. Note that the dependence of the phase envelope on pore size presented above will be different for a pore with a circular cross-section, where $p^c = 2\sigma/r_m$, and $r_m = r_e$ on the entire phase envelope (i.e., including both the bubble point and dew point lines). This means that the bubble point line will be lower than that of an equal-size pore with square and triangular cross-sections. Additionally, the dew point line will also change with pore size instead of being size-independent like that for the pores with square or triangular cross-sections. A comprehensive analysis of the phase behavior for a pore with a circular cross-section was presented in Sandoval et al. [42]. Another interesting observation is that the critical point does not change with pore size and geometry as shown in Fig. 2a–b. This is because the interfacial tension (σ) and p^c become zero at the critical point for any pore. Finally, we note that though the above analyses are for the $p^c(s^l)$ formulation presented in Eqs. (7)–(8), the general dependence of the phase behavior on pore size and geometry should be similar when the other p^c formulations mentioned in Section 2.1.2 are considered.

In addition to p^c, including the competitive adsorption further modifies the phase envelope. Though the bubble point line is similar to that when only p^c is included, the dew point line shifts up as the pore becomes smaller (Fig. 2c–d). The bubble point line remains almost unchanged because the competitive adsorption has a minimal impact on the composition of the bulk fluid when the entire pore is filled by the liquid phase. Conversely, the dew point line shifts up because the bulk fluid becomes "lighter" (i.e., the molar ratio between lighter and heavier components increases) resulting from preferential adsorption of heavier components to the pore walls. This adsorption-induced "stripping" effect becomes stronger in smaller pores. This is because the relative importance of adsorption scales with the ratio between the volume of the adsorbed phase and the total volume of the pore, and this ratio (approximately equal to the specific surface area, i.e., the surface area per unit pore volume) becomes greater as the pore size decreases. Additionally, due to the pore size-dependent "stripping" effect, the critical point now changes with pore size—the fluid in a smaller pore has a smaller critical temperature, but greater critical pressure. Finally, Fig. 2c–d also show that including the competitive adsorption does not change the dependence of the phase envelope on pore geometry. This can be explained by the fact that equal-size pores with square and triangular cross-sections have similar ratios between the volume of the adsorbed phase and the total volume of the pore—their specific surface areas are the same.

3.2. Phase behavior in complex nanopore networks

3.2.1. Phase behavior in a two-scale pore network

We simulate the phase behavior of hydrocarbons in a two-scale pore network that consists of one large pore (r_p = 100 nm) and 100

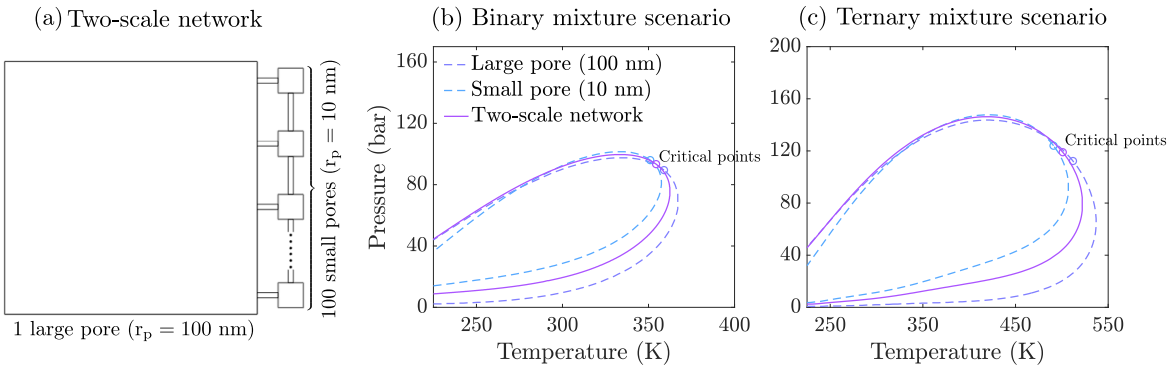

Fig. 3. (a) Schematic of the two-scale pore network that consists of one large pore (r_p = 100 nm) and 100 small pores (r_p = 10 nm). (b) and (c) show the macroscopic phase envelopes for the two-scale pore network (solid lines) for the binary and ternary mixture scenarios, respectively. The phase envelopes for the single nanopores (dash lines) are also presented for comparison. The critical points are labeled on the phase envelopes.

small pores (r_p = 10 nm). The pores are well-connected by throats as shown in Fig. 3a. To focus our analyses on the impact of pore sizes, we assume that the pores have the same geometry, i.e., they are all tubes with square cross-sections. The same binary and ternary hydrocarbon mixtures presented in Section 2.1 are simulated.

Fig. 3b–c presents the macroscopic phase envelopes for the network under both mixture scenarios. The phase envelope in a single pore (r_p = 10 nm and 100 nm) is also presented for comparison. The results show that the phase envelope of the network falls between the two single-pore phase envelopes. The critical point also falls between the two single-pore critical points. This is resulting from the fact that the adsorption-induced "stripping" effect (see Section 2.1) in the two-scale network is weaker than that in a single pore of r_p = 10 nm while stronger than that in a single pore of r_p = 100 nm. Another interesting observation is that the bubble point branch of the phase envelope for the two-scale network is closer to that of the large pore—they almost overlap except for when it is close to the critical points. This is because, at the bubble point, (1) the capillary pressure of the two-scale network is equal to σ/r_e where r_e is the effective radius of the large pore, i.e., the capillary pressure of the two-scale network is close to that of the large pore at the bubble point line; and (2) the "stripping" effect, though stronger in the two-scale network, has a minimal impact on the phase envelope at the bubble point line.

Inspection of the distribution of the fluid phases and components in the network leads to the following observations (Fig. 4). For both the binary and ternary mixture scenarios, the bulk phases and the total mass (bulk phases plus the adsorbed phase) in the small pores (r_p = 10 nm) are both denser than those in the large pore (r_p = 100 nm), i.e., the small pores have a greater ratio of heavier to lighter components than that in the large pore. This can be shown by the binary mixture scenario as an example. We examine two different conditions that correspond to a lower and a higher liquid saturation in the network, i.e., P^v = 70 bar and P^v = 90 bar at T = 330 K. When P^v = 70 bar (Fig. 4a), the molar ratios of C4 to C1 in the bulk phases and the total mass of all three phases in the small pore (1.22 and 1.33) are both greater than those in the large pore (0.64 and 0.64). Similarly, when P^v = 90 bar (Fig. 4c), the molar ratios of C4 to C1 in the small pore are 1.38 and 1.56 in the bulk phases and the total mass of all three phases, respectively, while those in the large pore are, respectively, 0.33 and 0.35. The above observations are a result of two mechanisms—capillary trapping and preferential adsorption of heavier components. Capillary trapping leads to more liquid residing in the small pore and the liquid phase has a greater molar ratio of heavier to lighter components than that of the vapor phase. Concomitantly, heavier components are more preferentially adsorbed to pore walls, which leads to a greater molar ratio of heavier to lighter components in the adsorbed phase than that in the bulk phases. Because the adsorbed phase accounts for a greater fraction of the total mass in the small pores (due to their greater specific surface area), the preferential adsorption of heavier components increases the molar ratio of heavier to lighter components. Consequently, the bubble point pressure in the small pores is significantly suppressed, i.e., the pressure at which the vapor phase first shows up in the small pores is much smaller than that in the large pore.

3.2.2. Phase behavior in multiscale pore networks

To examine the macroscopic phase behavior in more complex pore structures, we simulate the phase behavior of the hydrocarbon mixtures from Section 3.2.1 in two multiscale pore networks, denoted as multiscale network #1 and #2 (see Fig. 5a and d). The networks are unstructured with 100 × 100 × 100 pores and were generated using a method commonly used in previous studies [73,74]. The pore size follows a truncated lognormal distribution (normalized standard deviation is 0.5) and ranges from 5.5 nm to 100 nm (see Fig. 5b and e). The two networks have different average pore sizes (12.2 nm and 22.7 nm for multiscale networks #1 and #2, respectively). The pores are interconnected by throats and the average number of throats connecting to each pore (i.e., the average coordination number) is 4.3 in each network. All the pores and throats are assumed tubes with square cross-sections. A pore network has a macroscopic P^c-S^l curve that is a function of the detailed pore structures. The P^c-S^l curves for the two networks are shown in Fig. 5c and f (an interfacial tension of σ = 0.02 N/m was used for demonstration).

We present the macroscopic phase envelopes for the multiscale networks in Fig. 6. The phase envelope in a single pore (r_p = 5.5 nm and 100 nm) is also presented for comparison. The bubble point lines for the two networks almost overlap because they are both controlled by the capillary pressure of the largest pore as was discussed in Section 3.2.1. Conversely, their dew point lines—though both fall between the phase envelopes for the two single pores—are different from each other. A closer inspection reveals that the dew point line for multiscale network #1 is closer to that of r_p = 5.5 nm, while the dew point line for multiscale network #2 is closer to that of r_p = 100 nm. This is a direct result of the different pore size distributions of the two networks—though their pore sizes both follow a truncated log-normal distribution with the same normalized standard deviation, multiscale network #1 has an average pore size smaller than that of multiscale network #2 leading to a stronger "stripping" effect for the former.

We also present the spatial distribution of fluid phases and components in the two multiscale pore networks for the binary and ternary mixture scenarios in Figs. 7 and 8, respectively. Four different conditions are used as examples—P^v = 30, 50, 70, 90 bar; and T = 330 K for the binary mixture scenario and T = 450 K for the ternary mixture scenario. The results show that the multiscale pore structure controls the spatial distribution of liquid and vapor phases due to capillary trapping, i.e., the liquid phase tends to reside in the smaller pores.

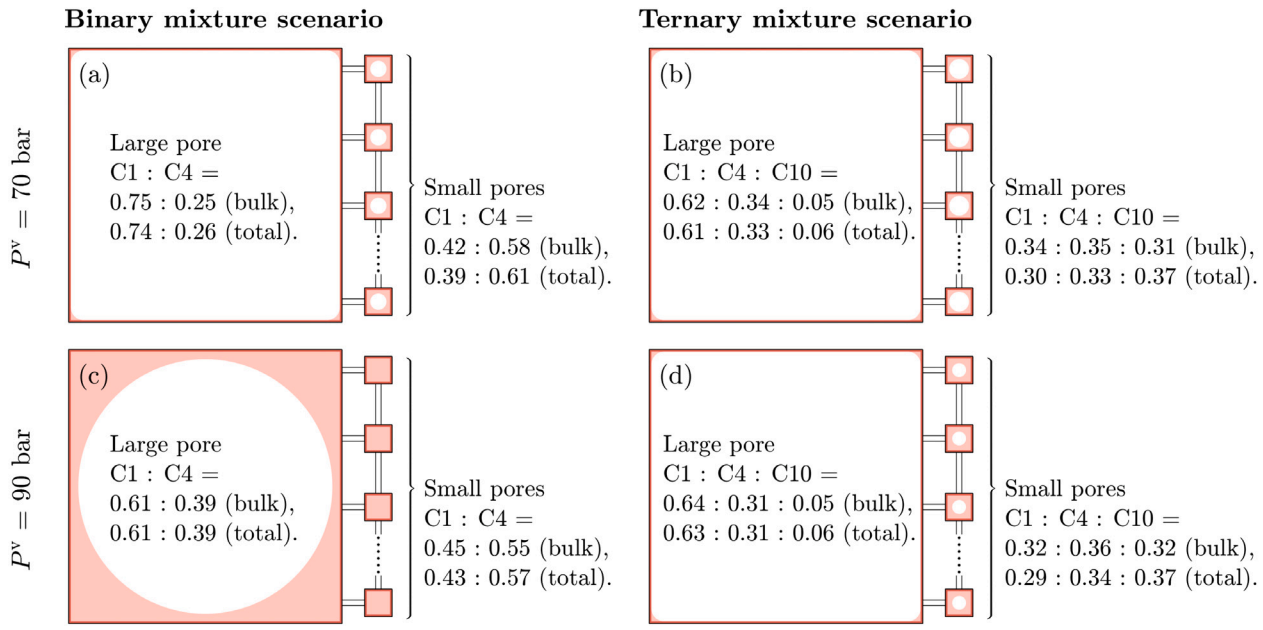

Fig. 4. Distribution of fluid phases and components in the two-scale network for the binary and ternary mixture scenarios. The adsorbed, liquid, and vapor phases are indicated by dark red, light red, and white colors, respectively. The compositions in liquid and vapor phases (denoted by "bulk") and in the total mass of all three phases (denoted by "total") are also presented.

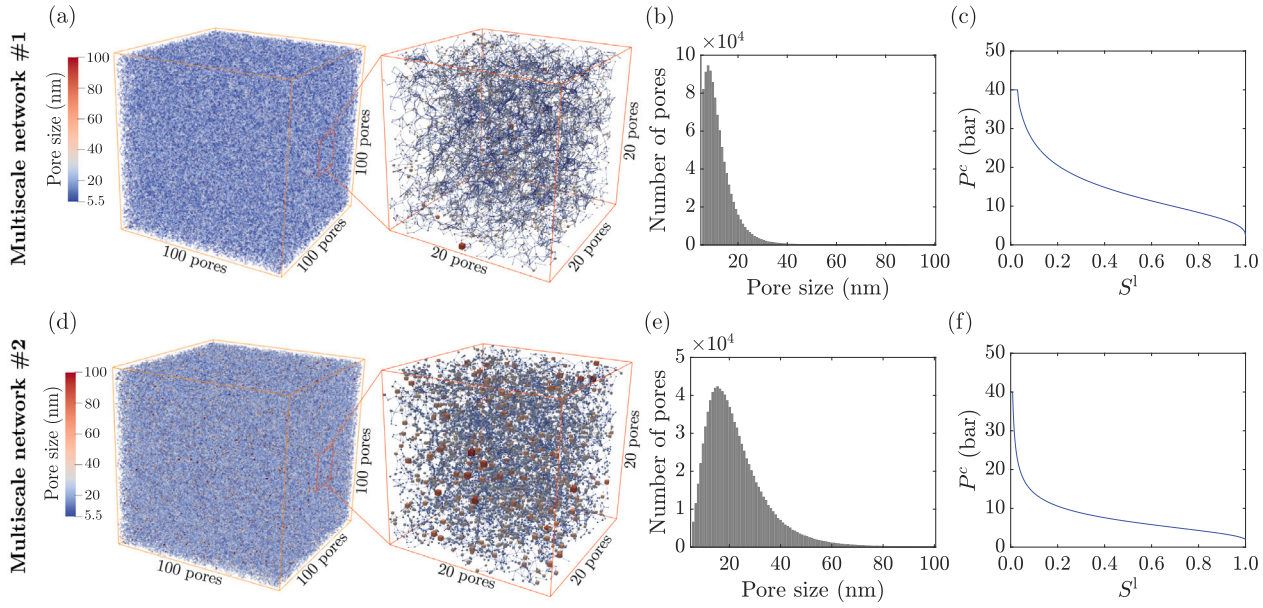

Fig. 5. The three-dimensional representation, pore size distribution, and the capillary pressure as a function of the liquid phase saturation P^c-S^l for (*a–c*) multiscale network #1 and (*d–f*) multiscale network #2. Each network consists of approximately 1,000,000 pores.

Because the liquid phase has a greater molar ratio of heavier to lighter components than that of the vapor phase, greater liquid phase saturation in the smaller pores leads to a greater molar ratio of heavier components. In addition, the multiscale pore structure also modifies the spatial distribution of the adsorbed phase. Namely, due to the greater specific surface area, the adsorbed phase in the smaller pores accounts for a greater fraction of the total mass of the three phases. Since the adsorbed phase has the greatest molar ratio of heavier to lighter components among all three phases, this also increases the molar ratio of heavier to lighter components in the smaller pores. Consequently, the bubble point pressure in the smaller pores is suppressed and the extent of suppression becomes greater as the pore size becomes smaller. We also note that the above observations regarding how the multiscale pore structure controls the distributions of phases and components and the bubble point pressure are consistent with those in the two-scale network in Section 3.2.1. Overall, the network-scale simulations presented here and in Section 3.2.1 all demonstrate that the multiscale pore structure (e.g., pore size distribution) is a primary factor that controls the macroscopic phase behavior and mass distribution in pore networks.

4. Discussion

We have developed a novel upscaling framework for deriving the macroscopic thermodynamic phase behavior of hydrocarbon mixtures in complex nanopore networks. The upscaling procedure involves the

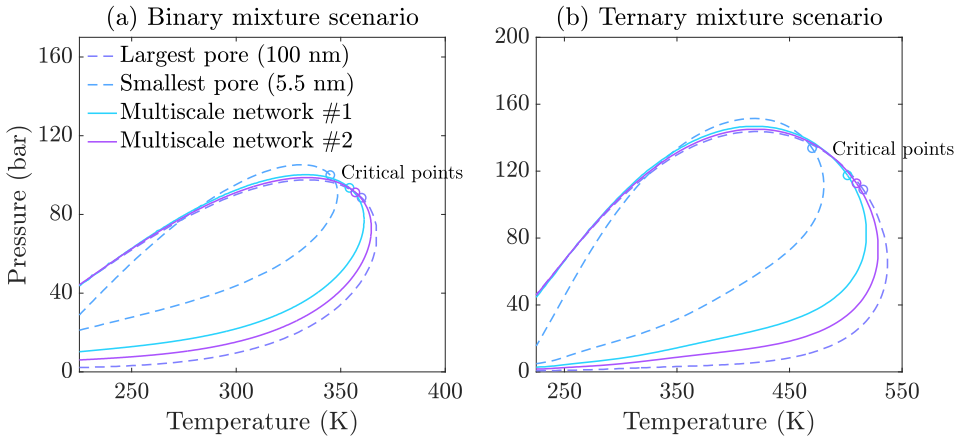

Fig. 6. Macroscopic phase envelopes (solid line) and critical points (circle) for multiscale network #1 and #2: (a) binary mixture scenario, (b) ternary mixture scenario. The phase envelopes (dash line) and critical points (circle) in a single nanopore—the largest pore (r_p = 100 nm) and the smallest pore (r_p = 5.5 nm) of the networks—are also presented for comparison.

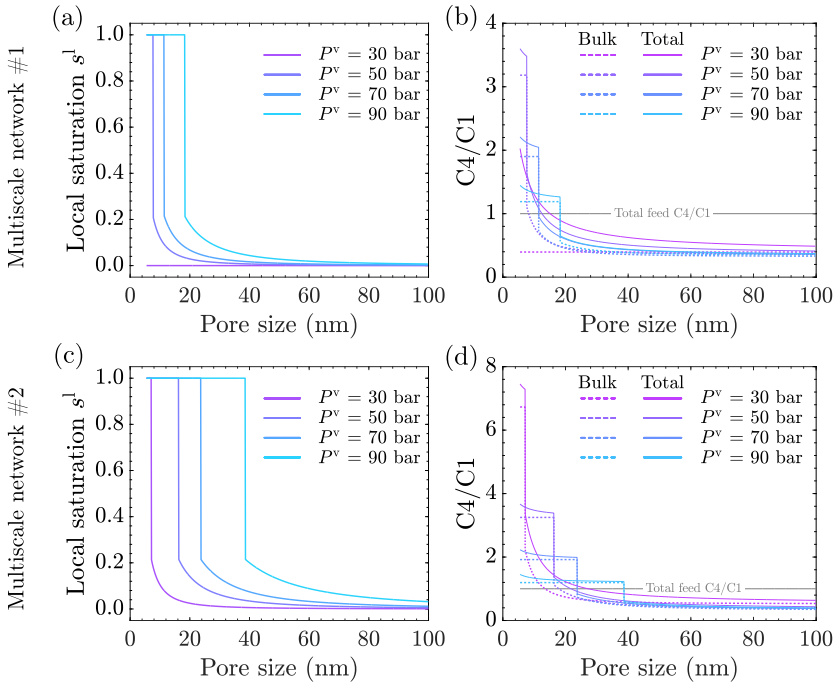

Fig. 7. The local liquid saturation and molar ratio of C4 to C1 in the individual pores for the binary mixture scenario in (*a-b*) multiscale network #1 and (*c-d*) multiscale network #2. Four example conditions (P^v = 30, 50, 70, 90 bar and T = 330 K) are presented. The *x*-axes in all plots denote the size of the pores in the networks. The *y*-axes in (*a*) and (*c*) denote the local liquid saturation in each pore, while the *y*-axes in (*b*) and (*d*) denote the local molar ratio of C4 to C1 in each pore in liquid and vapor phases (denoted by "Bulk", dash line) and in the total mass of all three phases (denoted by "Total", solid line).

following steps. Within each pore, we employ a generalized individual-pore phase equilibrium model that explicitly accounts for the capillary pressure and competitive adsorption of hydrocarbon components. Assuming thermodynamic equilibrium across the pore network, we derive the upscaled phase behavior variables for the entire pore network by integrating the variables from all individual pores. The end result is a network-scale phase equilibrium model that naturally accounts for the size- and geometry-dependent nanoconfinement effects of the complex nanopore structures.

We have applied the upscaled model to examine a wide range of factors—including capillary pressure, competitive adsorption, pore size, pore geometry, and pore size distribution—that may affect the macroscopic phase behavior in multiscale pore networks that consist of up to a million nanopores. It was shown that heavier components always preferentially reside in smaller pores as a result of capillary trapping of the liquid phase and preferential adsorption of the heavier components on the pore wall (see Section 3.2). The greater mole fraction of heavier components in the smaller pores suppresses their bubble point pressure and in turn modifies the macroscopic phase behavior of the entire network. These observations illustrate that the multiscale pore structure is a primary factor that controls the macroscopic phase behavior in a nanopore network.

The dependence of the nanoconfined phase behavior on the multiscale pore structures revealed in our simulations is in line with prior nanofluidic experiments [15] and advanced theoretical modeling studies [22,26,32–35]. Zhong et al. [15] employed nanofluidic experiments to examine the phase behavior of C1 and C3 mixtures in connected two-scale silicon nanochannels. The experimental observations and comparison to DFT simulations revealed that the bubble point in the smaller channels was suppressed by approximately 3 folds due to capillarity and competitive surface adsorption. Several more comprehensive DFT studies [32–35] that simulated constant composition expansion

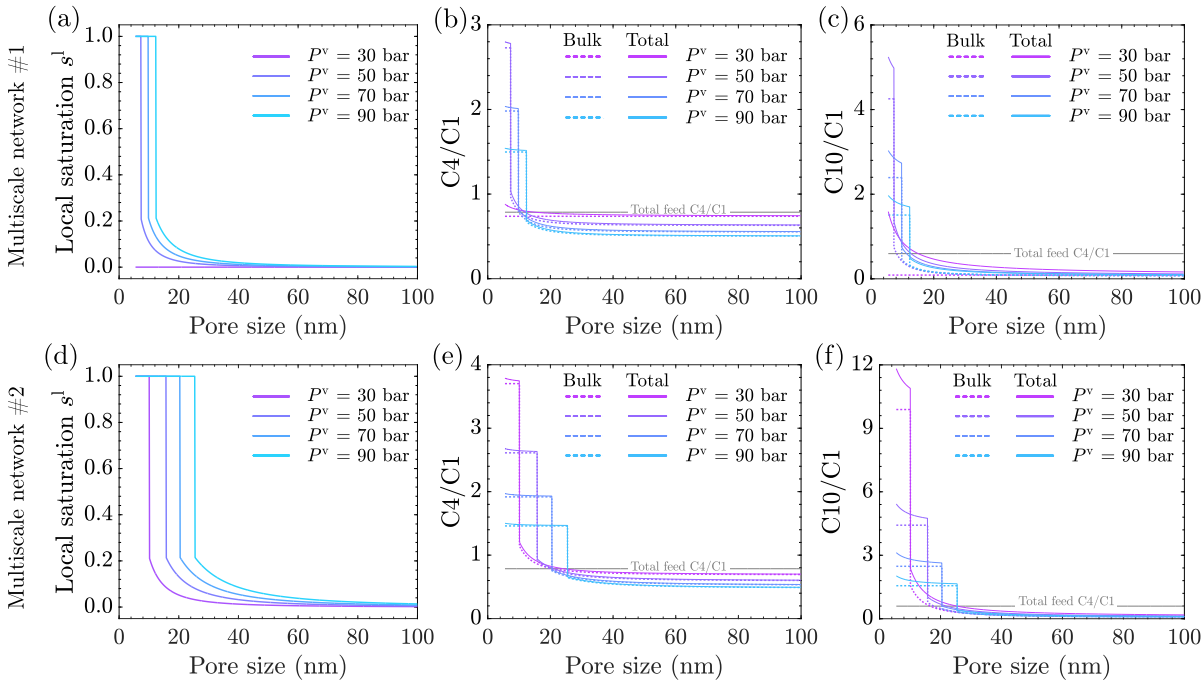

Fig. 8. The local liquid saturation, molar ratios of C4 to C1 and C10 to C1 for the ternary mixture scenario in (*a*–*c*) multiscale network #1 and (*d*–*f*) multiscale network #2. Four example conditions ($P^v = 30, 50, 70, 90$ bar and $T = 450$ K) are presented. The *x*-axes in all plots denote the size of the pores in the networks. The *y*-axes in (*a*) and (*d*) denote the local liquid saturation in each pore. The *y*-axes in (*b*) and (*e*) denote the local molar ratio of C4 to C1 in each pore, and *y*-axes in (*c*) and (*f*) denote the local molar ratio of C10 to C1 in each pore. The dash line represents the molar ratio in liquid and vapor phases (denoted by "Bulk"), while the solid line represents the molar ratio in total mass of all three phases (denoted by "Total").

and constant volume depletion in multiscale systems—consisting of one or several carbon-slit nanopores and a fracture (bulk)—further quantified the impact of competitive surface adsorption on the phase behavior in the nanopores. Similarly, the impact of the multiscale pore structure on the nanoconfined phase behaviors has also been independently observed in GEMC or MD simulations for more complex mixtures (up to 8 components) and solid materials (e.g., silica, kerogen, and graphite) in two-scale systems [22,26].

More generally, the present upscaling framework can be integrated into the workflow of digital rock physics for deriving macroscopic phase behavior parameters for realistic pore networks in shale rocks. Digital rock physics refer to the general workflow that uses high-resolution images of rock samples as inputs for deriving macroscopic properties or for numerical simulations of different physical and chemical processes, e.g., gas transport or multiphase flow [e.g., 60,75–77]. For shale rocks specifically, advanced imaging techniques including X-ray computed tomography and focused ion beam scanning electron microscopy can be employed to acquire high-resolution images of the pore structures [e.g., 77–80]. Algorithms such as watershed segmentation [81–84], maximal ball [85–87], and axial skeleton [88,89] can then be used to extract pore networks that replicate the key pore structural properties of the rock samples (e.g., pore size, shape factor, surface area, and connectivity). Once a pore network is obtained, our upscaling framework can be directly employed to derive parameters for the macroscopic phase behavior model for a rock sample. From a practical standpoint, because the macroscopic phase behavior formulation shares the same mathematical structure as that of a standard bulk phase behavior model (see Section 2.2), it can be readily incorporated in any standard reservoir simulators [90–95].

In addition, the upscaling framework can be extended to model a wider range of conditions such as more complex fluids (i.e., the presence of other fluids in addition to hydrocarbons) and heterogeneous rocks. Non-polar components (e.g., CO_2) that dissolve in hydrocarbons can be directly included if the thermodynamic properties (e.g., critical pressure, and critical temperature) and adsorption parameters (e.g., maximum adsorption, adsorption equilibrium constant, and adsorption thickness) are available [48,96]. For polar components (e.g., H_2O) that have limited miscibility in hydrocarbons, a separate phase in addition to the hydrocarbon phases may appear. This would require a further modification to the phase behavior model to account for thermodynamic equilibrium between hydrocarbon phases and the new separate phase [61, ch. 16]. In addition to more complex fluids, our framework also allows for different contact angles in the different pores to account for spatially variable wettability in shale rocks. Here, we illustrate this capability using a two-pore network as an example (see Appendix A.3). The two pores are identical except that they have different wettabilities (i.e., their contact angles θ are different). Preliminary results demonstrate that the variable wettability can also modify the nanoconfined phase behavior—more liquid is trapped in the pore with a smaller contact angle, leading to a greater mole fraction of heavier components that suppresses the bubble point pressure.

Finally, we point out that the upscaling framework may be further extended to include several additional factors that have not been examined in the present work. The current framework assumes that (1) the capillary pressure follows the standard Young–Laplace equation, (2) the adsorption can be modeled by the relatively simple ML model, and (3) the adsorbed phase has a uniform thickness and density. While these assumptions are expected to be valid for the range of pore sizes in the present work ($r_p \geq 5.5$ nm) [14,27,59,71,72], some of them might break down for smaller pores. For example, the capillary pressure may deviate from the prediction of the standard Young–Laplace equation due to strong interactions between the liquid-vapor interfaces and the solid surface [97–99]. Additionally, the adsorbed phase may not have a uniform depth and density due to the inhomogeneous fluid-wall interaction. As the pore size becomes even smaller (e.g., sub 1 nm), a fluid may not be considered as a continuum and thus phase transition may not be defined. To account for the above anomalous behaviors in small nanopores, more generalized capillary pressure, adsorption, and phase behavior models may be derived using advanced theoretical models such as MD, GCMC, GEMC, and DFT [23,24,99–102]. We note that because these generalized models will only modify the local

phase equilibrium model in each individual pore, they can be directly incorporated in the current upscaling framework to further examine the nanoconfined phase behavior in smaller pores.

5. Conclusion

We have developed a novel upscaling framework for deriving the macroscopic phase behavior of hydrocarbon mixtures in realistic nanopore networks in shale rocks. The upscaled phase behavior model accounts for the pore size- and geometry-dependent nanoconfinement effects of pores varying in geometry and whose size spans several order of magnitude. The main contributions of the present work are summarized as follows.

(1) A novel upscaling framework has been developed for the thermodynamic phase behavior of hydrocarbon mixtures in the complex pore networks of shale rocks.

(2) Simulations using the upscaled model demonstrate that the multiscale pore structure is a primary factor that governs the macroscopic phase behavior in the shale rocks. Resulting from capillary trapping of the liquid phase and competitive adsorption on the pore wall, heavier components tend to reside in smaller pores and thus the bubble point pressure is suppressed in those pores. These observations are supported by prior studies using nanofluidic experiments and advanced theoretical models including MD, GEMC, and DFT.

(3) The new upscaling framework, when combined with digital rock physics, provides a workflow for parameterizing the macroscopic phase behavior formulations for shale rocks. Further more, the upscaled phase behavior formulation shares the same computational structure as that of a standard bulk phase behavior formulation and can be readily incorporated in commercial reservoir simulators for field-scale applications.

Declaration of competing interest

The authors declare that they have no known competing financial interests or personal relationships that could have appeared to influence the work reported in this paper.

Acknowledgment

This work was supported by the Water, Environmental, and Energy Solutions (WEES) Initiative at the University of Arizona, USA. We thank Dr. Chaozhong Qin for providing the code to generate the multiscale pore networks.

Appendix

A.1. Relationships among the macroscopic principle radius of curvature R_m, macroscopic liquid saturation S^{l}, and local saturation s^{l}

Fig. A.1 presents the macroscopic principle radius of curvature R_m corresponding to different macroscopic liquid saturation S^{l} as revealed by Eq. (30). Once S^{l} and R_m are known, the local saturation s^{l} in a pore network can be computed accordingly, which is presented as follows. When $S^{\mathrm{l}} \le S^{\mathrm{l}}_0$, we assume the menisci of fluid-fluid interfaces are uniform in all pores. Thus the volume of liquid phase in each pore scales with the pore length and s^{l} can be computed by the ratio of the volume of liquid phase to the volume of liquid and vapor phases. When $S^{\mathrm{l}} > S^{\mathrm{l}}_0$ and pore i is the smallest unsaturated pore, then (1) pores whose size is smaller than pore i have $s^{\mathrm{l}} = 1$; (2) pores whose size is equal to pore i have the same s^{l}; (3) pores whose size is greater than pore i have $s^{\mathrm{l}} < s^{\mathrm{l}}_c$ and $r_m = R_m$, so that their s^{l} is a function of R_m which is a function of S^{l}

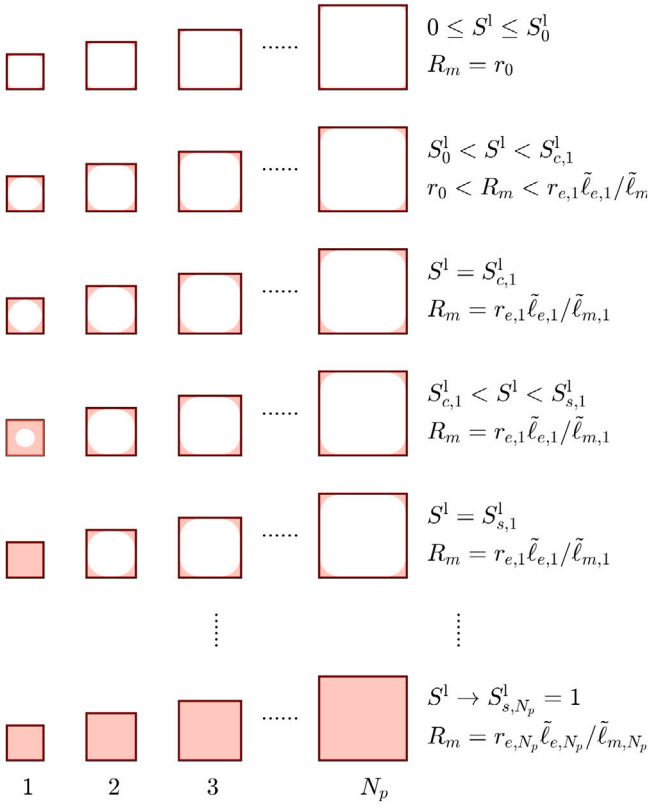

Fig. A.1. Relationships among the macroscopic principle radius of curvature R_m, macroscopic liquid saturation S^{l}, and local liquid saturation s^{l}. For demonstration purposes, pores with square cross-sections are used here. Each row represents a different S^{l} in the pore network and S^{l} increases from top to bottom. In each row, the size of the pores (the pore network has N_p pores in total) increases from left to right. Within each pore, the adsorbed, liquid, and vapor phases are indicated by dark red, light red, and white colors, respectively. If multiple pores have the same size, they will have the same saturation.

(see Eq. (30) for the R_m-S^{l} relationship). Finally, the general expression of s^{l} in each pore j of the network can be given by

$$s^{\mathrm{l}}_j = \begin{cases} \dfrac{\ell_j S^{\mathrm{l}}(V - V^{\mathrm{ad}})}{\left(\sum_{j'=1}^{N_p} \ell_{j'}\right)(v_j - v^{\mathrm{ad}}_j)} & S^{\mathrm{l}} \le S^{\mathrm{l}}_0, \\ 1 & S^{\mathrm{l}} > S^{\mathrm{l}}_0 \,\&\, r_{e,j} < r_{e,i}, \\ \dfrac{S^{\mathrm{l}}(V - V^{\mathrm{ad}}) - \left(\sum_{j'=1}^{i-1}(v_{j'} - v^{\mathrm{ad}}_{j'}) + \sum_{j'=i+n_i}^{N_p} \ell_{j'}\tilde{a}_{m,j'}R^2_m\right)}{\sum_{j'=i}^{i+n_i-1}(v_{j'} - v^{\mathrm{ad}}_{j'})} & S^{\mathrm{l}} > S^{\mathrm{l}}_0 \,\&\, r_{e,j} = r_{e,i}, \\ \ell_j \tilde{a}_{m,j} R^2_m/(v_j - v^{\mathrm{ad}}_j) & S^{\mathrm{l}} > S^{\mathrm{l}}_0 \,\&\, r_{e,j} > r_{e,i}, \end{cases} \tag{A.1}$$

where n_i denotes the number of pores that have the same size as that of pore i (including pore i).

A.2. Verification of model implementation for a single nanopore with a circular cross-section

We compare our individual-pore phase equilibrium model to that of Sandoval et al. [59] for a pore with a circular cross-section (r_p = 10 nm) to verify our implementation (see Fig. A.2). Note that because the radius of curvature of the liquid-vapor interfaces was computed by assuming $h = 0$ in Sandoval et al. [59], we set the volume (v^{ad}) and thickness (h) of the adsorbed phase to zero for the simulations presented here, except for the v^{ad} in Eq. (15).

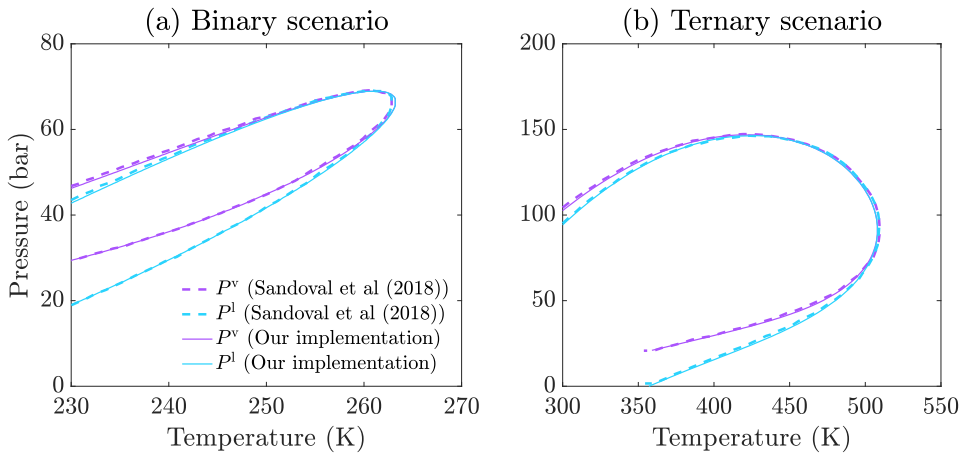

Fig. A.2. Validation of the model implementation by comparing the phase envelopes of a binary mixture (C1 : C2 = 0.5 : 0.5) and a ternary mixture (C1 : C4 : C10 = 0.42 : 0.33 : 0.25) in a single nanopore with a circular cross-section (r_p = 10 nm) with those obtained by Sandoval et al. [59].

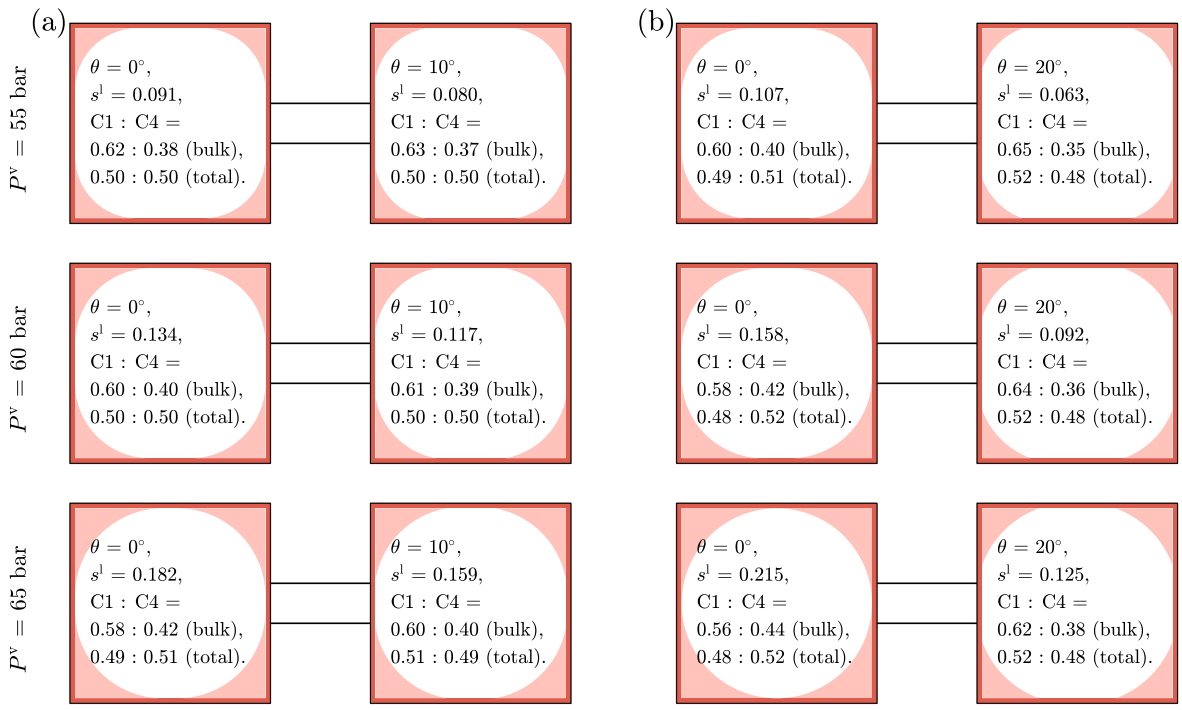

Fig. A.3. Distribution of fluid phases and components in a two-pore network with different wettability: (a) two pores have contact angles of 0° and 10°, (b) two pores have contact angles of 0° and 20°. The adsorbed, liquid, and vapor phases are indicated by dark red, light red, and white colors, respectively. The compositions in liquid and vapor phases (denoted by "bulk") and in the total mass of all three phases (denoted by "total") are also presented.

A.3. Extending the current framework for pore networks with spatially variable wettability

We demonstrate that the current framework can be extended for pore networks with spatially variable wettability. A two-pore network is used as an example. The two pores are constructed to be identical except that their contact angles are different. We simulate two scenarios: the first assumes that the two pores have contact angles of 0° and 10°, while the second assumes the two pores have contact angles of 0° and 20°. A binary mixture (C1 : C4 = 0.5 : 0.5) under three different conditions corresponding to a relatively low, moderate, high liquid saturation in the network, i.e., P^v = 55, 60, 65 bar at T = 330 K, are simulated. The distributions of fluid phases and components in the pore network are presented in Fig. A.3. The results show that, in addition to the pore size, the variable wettability also modifies the nanoconfined phase behavior. Specifically, more liquid is trapped in the pore with a smaller contact angle, leading to a greater mole fraction of heavier components. This difference becomes greater as the contact angles of the two pores become more different (i.e., the wettability becomes more heterogeneous).

References

[1] EIA, Annual energy outlook, U.S. Energy Information Administration, 2020, https://www.eia.gov/outlooks/aeo/.
[2] C.H. Whitson, S. Sunjerga, PVT in liquid-rich shale reservoirs, in: SPE Annual Technical Conference and Exhibition, Society of Petroleum Engineers, 2012.
[3] B. Nojabaei, R.T. Johns, L. Chu, Effect of capillary pressure on phase behavior in tight rocks and shales, SPE Reserv. Eval. Eng. 16 (03) (2013) 281–289.
[4] S. Luo, J.L. Lutkenhaus, H. Nasrabadi, Experimental study of confinement effect on hydrocarbon phase behavior in nano-scale porous media using differential scanning calorimetry, in: SPE Annual Technical Conference and Exhibition, Society of Petroleum Engineers, 2015.

[5] M. Khoshghadam, W.J. Lee, A. Khanal, Numerical study of impact of nano-pores on gas-oil ratio and production mechanisms in liquid-rich shale oil reservoirs, in: Unconventional Resources Technology Conference (URTEC), 2015.
[6] A. Cihan, T.K. Tokunaga, J.T. Birkholzer, Adsorption and capillary condensation-induced imbibition in nanoporous media, Langmuir 35 (29) (2019) 9611–9621.
[7] T.W. Teklu, N. Alharthy, H. Kazemi, X. Yin, R.M. Graves, A.M. AlSumaiti, Phase behavior and minimum miscibility pressure in nanopores, SPE Reserv. Eval. Eng. 17 (03) (2014) 396–403.
[8] B.T. Bui, H.-H. Liu, J. Chen, A.N. Tutuncu, Effect of capillary condensation on gas transport in shale: A pore-scale model study, SPE J. 21 (02) (2016) 601–612.
[9] E. Barsotti, S.P. Tan, S. Saraji, M. Piri, J.-H. Chen, A review on capillary condensation in nanoporous media: Implications for hydrocarbon recovery from tight reservoirs, Fuel 184 (2016) 344–361.
[10] T. Pitakbunkate, T. Blasingame, G. Moridis, P. Balbuena, Phase behavior of methane-ethane mixtures in nanopores, Ind. Eng. Chem. Res. 56 (40) (2017) 11634–11643.
[11] E. Parsa, X. Yin, E. Ozkan, Direct observation of the impact of nanopore confinement on petroleum gas condensation, in: SPE Annual Technical Conference and Exhibition, Society of Petroleum Engineers, 2015.
[12] M. Alfi, H. Nasrabadi, D. Banerjee, Experimental investigation of confinement effect on phase behavior of hexane, heptane and octane using lab-on-a-chip technology, Fluid Phase Equilib. 423 (2016) 25–33.
[13] B. Bao, J. Riordon, F. Mostowfi, D. Sinton, Microfluidic and nanofluidic phase behaviour characterization for industrial CO2, oil and gas, Lab Chip 17 (16) (2017) 2740–2759.
[14] J. Zhong, J. Riordon, S.H. Zandavi, Y. Xu, A.H. Persad, F. Mostowfi, D. Sinton, Capillary condensation in 8 nm deep channels, J. Phys. Chem. Lett. 9 (3) (2018) 497–503.
[15] J. Zhong, Y. Zhao, C. Lu, Y. Xu, Z. Jin, F. Mostowfi, D. Sinton, Nanoscale phase measurement for the shale challenge: Multicomponent fluids in multiscale volumes, Langmuir 34 (34) (2018) 9927–9935.
[16] J. Zhong, M.A. Alibakhshi, Q. Xie, J. Riordon, Y. Xu, C. Duan, D. Sinton, Exploring anomalous fluid behavior at the nanoscale: Direct visualization and quantification via nanofluidic devices, Acc. Chem. Res. 53 (2) (2020) 347–357.
[17] B. Bao, S. Zhao, A review of experimental nanofluidic studies on shale fluid phase and transport behaviors, J. Nat. Gas Sci. Eng. (2020) 103745.
[18] B. Bao, J. Qiu, F. Liu, Q. Fan, W. Luo, S. Zhao, Capillary trapping induced slow evaporation in nanochannels, J. Pet. Sci. Eng. 196 (2021) 108084.
[19] A. Jatukaran, J. Zhong, A.H. Persad, Y. Xu, F. Mostowfi, D. Sinton, Direct visualization of evaporation in a two-dimensional nanoporous model for unconventional natural gas, ACS Appl. Nano Mater. 1 (3) (2018) 1332–1338.
[20] A. Jatukaran, J. Zhong, A. Abedini, A. Sherbatian, Y. Zhao, Z. Jin, F. Mostowfi, D. Sinton, Natural gas vaporization in a nanoscale throat connected model of shale: Multi-scale, multi-component and multi-phase, Lab Chip 19 (2) (2019) 272–280.
[21] W.R. Welch, M. Piri, Molecular dynamics simulations of retrograde condensation in narrow oil-wet nanopores, J. Phys. Chem. C 119 (18) (2015) 10040–10047.
[22] C. Herdes, C. Petit, A. Mejía, E.A. Muller, Combined experimental, theoretical, and molecular simulation approach for the description of the fluid-phase behavior of hydrocarbon mixtures within shale rocks, Energy Fuels 32 (5) (2018) 5750–5762.
[23] M. Sedghi, M. Piri, Capillary condensation and capillary pressure of methane in carbon nanopores: Molecular dynamics simulations of nanoconfinement effects, Fluid Phase Equilib. 459 (2018) 196–207.
[24] B. Jin, H. Nasrabadi, Phase behavior of multi-component hydrocarbon systems in nano-pores using gauge-GCMC molecular simulation, Fluid Phase Equilib. 425 (2016) 324–334.
[25] B. Jin, R. Bi, H. Nasrabadi, Molecular simulation of the pore size distribution effect on phase behavior of methane confined in nanopores, Fluid Phase Equilib. 452 (2017) 94–102.
[26] R. Bi, H. Nasrabadi, Molecular simulation of the constant composition expansion experiment in shale multi-scale systems, Fluid Phase Equilib. 495 (2019) 59–68.
[27] Z. Jin, A. Firoozabadi, Thermodynamic modeling of phase behavior in shale media, SPE J. 21 (01) (2016) 190–207.
[28] Z. Jin, Bubble/dew point and hysteresis of hydrocarbons in nanopores from molecular perspective, Fluid Phase Equilib. 458 (2018) 177–185.
[29] P.I. Ravikovitch, A.V. Neimark, Experimental confirmation of different mechanisms of evaporation from ink-bottle type pores: Equilibrium, pore blocking, and cavitation, Langmuir 18 (25) (2002) 9830–9837.
[30] N. Klomkliang, D.D. Do, D. Nicholson, Scanning curves in wedge pore with the wide end closed: Effects of temperature, AIChE J. 61 (11) (2015) 3936–3943.
[31] E. Lowry, M. Piri, Effects of chemical and physical heterogeneity on confined phase behavior in nanopores, Microporous Mesoporous Mater. 263 (2018) 53–61.
[32] Y. Zhao, Y. Wang, J. Zhong, Y. Xu, D. Sinton, Z. Jin, Bubble point pressures of hydrocarbon mixtures in multiscale volumes from density functional theory, Langmuir 34 (46) (2018) 14058–14068.
[33] Y. Zhao, Z. Jin, et al., Hydrocarbon-phase behaviors in shale nanopore/fracture model: Multiscale, multicomponent, and multiphase, SPE J. 24 (06) (2019) 2–526.
[34] Y. Wang, Z. Jin, Effect of pore size distribution on hydrocarbon mixtures adsorption in shale nanoporous media from engineering density functional theory, Fuel 254 (2019) 115650.
[35] Y. Zhao, Z. Jin, Hydrocarbon mixture phase behavior in multi-scale systems in relation to shale oil recovery: The effect of pore size distributions, Fuel 291 (2021) 120141.
[36] M.L. Michelsen, The isothermal flash problem. Part I. Stability, Fluid Phase Equilib. 9 (1) (1982) 1–19.
[37] M.L. Michelsen, The isothermal flash problem. Part II. Phase-split calculation, Fluid Phase Equilib. 9 (1) (1982) 21–40.
[38] L. Fisher, J. Israelachvili, Direct experimental verification of the kelvin equation for capillary condensation, Nature 277 (5697) (1979) 548–549.
[39] S. Luo, J.L. Lutkenhaus, H. Nasrabadi, Confinement-induced supercriticality and phase equilibria of hydrocarbons in nanopores, Langmuir 32 (44) (2016) 11506–11513.
[40] A. Brusilovsky, Mathematical simulation of phase behavior of natural multicomponent systems at high pressures with an equation of state, SPE Reserv. Eng. 7 (01) (1992) 117–122.
[41] A.A. Shapiro, E.H. Stenby, Thermodynamics of the multicomponent vapor–liquid equilibrium under capillary pressure difference, Fluid Phase Equilib. 178 (1–2) (2001) 17–32.
[42] D.R. Sandoval, W. Yan, M.L. Michelsen, E.H. Stenby, The phase envelope of multicomponent mixtures in the presence of a capillary pressure difference, Ind. Eng. Chem. Res. 55 (22) (2016) 6530–6538.
[43] M. Sherafati, K. Jessen, Stability analysis for multicomponent mixtures including capillary pressure, Fluid Phase Equilib. 433 (2017) 56–66.
[44] D.R. Sandoval, M.L. Michelsen, W. Yan, E.H. Stenby, Vt-based phase envelope and flash calculations in the presence of capillary pressure, Ind. Eng. Chem. Res. 58 (13) (2019) 5291–5300.
[45] B. Stimpson, M. Barrufet, Constructing oil/gas capillary pressure and relative permeability curves from a distribution of pores in shale reservoirs, in: Unconventional Resources Technology Conference, Austin, Texas, 24-26 July 2017, Society of Exploration Geophysicists, American Association of Petroleum Geologists, Society of Petroleum Engineers, 2017, pp. 1035–1054.
[46] L. Wang, X. Yin, K.B. Neeves, E. Ozkan, Effect of pore-size distribution on phase transition of hydrocarbon mixtures in nanoporous media, SPE J. 21 (06) (2016) 1–981.
[47] W. Song, L. Liu, D. Wang, Y. Li, M. Prodanović, J. Yao, Nanoscale confined multicomponent hydrocarbon thermodynamic phase behavior and multiphase transport ability in nanoporous material, Chem. Eng. J. 382 (2020) 122974.
[48] S. Chen, C. Qin, B. Guo, Fully implicit dynamic pore-network modeling of two-phase flow and phase change in porous media, Water Resour. Res. (2020) e2020WR028510.
[49] S. Luo, J.L. Lutkenhaus, H. Nasrabadi, Multiscale fluid-phase-behavior simulation in shale reservoirs using a pore-size-dependent equation of state, SPE Reserv. Eval. Eng. 21 (04) (2018) 806–820.
[50] S. Luo, J.L. Lutkenhaus, H. Nasrabadi, Effect of nanoscale pore-size distribution on fluid phase behavior of gas-improved oil recovery in shale reservoirs, SPE J. (2020).
[51] M. Thommes, G.H. Findenegg, Pore condensation and critical-point shift of a fluid in controlled-pore glass, Langmuir 10 (11) (1994) 4270–4277.
[52] L.D. Gelb, K. Gubbins, R. Radhakrishnan, M. Sliwinska-Bartkowiak, Phase separation in confined systems, Rep. Progr. Phys. 62 (12) (1999) 1573.
[53] A.V. Neimark, P.I. Ravikovitch, A. Vishnyakov, Bridging scales from molecular simulations to classical thermodynamics: Density functional theory of capillary condensation in nanopores, J. Phys.: Condens. Matter 15 (3) (2003) 347.
[54] G.J. Zarragoicoechea, V.A. Kuz, Critical shift of a confined fluid in a nanopore, Fluid Phase Equilib. 220 (1) (2004) 7–9.
[55] S.K. Singh, A. Sinha, G. Deo, J.K. Singh, Vapor-liquid phase coexistence, critical properties, and surface tension of confined alkanes, J. Phys. Chem. C 113 (17) (2009) 7170–7180.
[56] T. Pitakbunkate, P.B. Balbuena, G.J. Moridis, T.A. Blasingame, et al., Effect of confinement on pressure/volume/temperature properties of hydrocarbons in shale reservoirs, SPE J. 21 (02) (2016) 621–634.
[57] L. Travalloni, M. Castier, F.W. Tavares, S.I. Sandler, Thermodynamic modeling of confined fluids using an extension of the generalized van der waals theory, Chem. Eng. Sci. 65 (10) (2010) 3088–3099.
[58] L. Travalloni, M. Castier, F.W. Tavares, Phase equilibrium of fluids confined in porous media from an extended peng-robinson equation of state, Fluid Phase Equilib. 362 (2014) 335–341.
[59] D.R. Sandoval, W. Yan, M.L. Michelsen, E.H. Stenby, Influence of adsorption and capillary pressure on phase equilibria inside shale reservoirs, Energy Fuels 32 (3) (2018) 2819–2833.
[60] M.J. Blunt, B. Bijeljic, H. Dong, O. Gharbi, S. Iglauer, P. Mostaghimi, A. Paluszny, C. Pentland, Pore-scale imaging and modelling, Adv. Water Resour. 51 (2013) 197–216.
[61] K.S. Pedersen, P.L. Christensen, J.A. Shaikh, P.L. Christensen, Phase Behavior of Petroleum Reservoir Fluids, CRC Press, 2006.

[62] S. Ma, G. Mason, N.R. Morrow, Effect of contact angle on drainage and imbibition in regular polygonal tubes, Colloids Surf. A 117 (3) (1996) 273–291.
[63] K.E. Thompson, Pore-scale modeling of fluid transport in disordered fibrous materials, AIChE J. 48 (7) (2002) 1369–1389.
[64] V. Joekar-Niasar, S.M. Hassanizadeh, H. Dahle, Non-equilibrium effects in capillarity and interfacial area in two-phase flow: Dynamic pore-network modelling, J. Fluid Mech. 655 (2010) 38.
[65] D.-Y. Peng, D.B. Robinson, A new two-constant equation of state, Ind. Eng. Chem. Fundam. 15 (1) (1976) 59–64.
[66] J.S. Lopez-Echeverry, S. Reif-Acherman, E. Araujo-Lopez, Peng-robinson equation of state: 40 years through cubics, Fluid Phase Equilib. 447 (2017) 39–71.
[67] D.R. Sandoval, W. Yan, M.L. Michelsen, E.H. Stenby, Modeling of shale gas adsorption and its influence on phase equilibrium, Ind. Eng. Chem. Res. 57 (17) (2017) 5736–5747.
[68] H. Cárdenas, E.A. Müller, How does the shape and surface energy of pores affect the adsorption of nanoconfined fluids?, AIChE J. (2020) e17011.
[69] G. McGonigal, R. Bernhardt, D. Thomson, Imaging alkane layers at the liquid/graphite interface with the scanning tunneling microscope, Appl. Phys. Lett. 57 (1) (1990) 28–30.
[70] S. Wang, Q. Feng, F. Javadpour, T. Xia, Z. Li, Oil adsorption in shale nanopores and its effect on recoverable oil-in-place, Int. J. Coal Geol. 147 (2015) 9–24.
[71] Q. Yang, B. Jin, D. Banerjee, H. Nasrabadi, Direct visualization and molecular simulation of dewpoint pressure of a confined fluid in sub-10 nm slit pores, Fuel 235 (2019) 1216–1223.
[72] Y. Wang, N. Shardt, C. Lu, H. Li, J.A. Elliott, Z. Jin, Validity of the kelvin equation and the equation-of-state-with-capillary-pressure model for the phase behavior of a pure component under nanoconfinement, Chem. Eng. Sci. 226 (2020) 115839.
[73] C. Qin, B. Guo, M. Celia, R. Wu, Dynamic pore-network modeling of air-water flow through thin porous layers, Chem. Eng. Sci. 202 (2019) 194–207.
[74] C. Qin, H. van Brummelen, A dynamic pore-network model for spontaneous imbibition in porous media, Adv. Water Resour. (2019) 103420.
[75] D. Wildenschild, C. Vaz, M. Rivers, D. Rikard, B. Christensen, Using X-ray computed tomography in hydrology: Systems, resolutions, and limitations, J. Hydrol. 267 (3–4) (2002) 285–297.
[76] T. Bultreys, W. De Boever, V. Cnudde, Imaging and image-based fluid transport modeling at the pore scale in geological materials: A practical introduction to the current state-of-the-art, Earth-Sci. Rev. 155 (2016) 93–128.
[77] B. Guo, L. Ma, H.A. Tchelepi, Image-based micro-continuum model for gas flow in organic-rich shale rock, Adv. Water Resour. 122 (2018) 70–84.
[78] M.E. Curtis, C.H. Sondergeld, R.J. Ambrose, C.S. Rai, Microstructural investigation of gas shales in two and three dimensions using nanometer-scale resolution imaging microstructure of gas shales, AAPG Bull. 96 (4) (2012) 665–677.
[79] G.R. Chalmers, R.M. Bustin, I.M. Power, Characterization of gas shale pore systems by porosimetry, pycnometry, surface area, and field emission scanning electron microscopy/transmission electron microscopy image analyses: Examples from the barnett, woodford, haynesville, marcellus, and doig units, AAPG Bull. 96 (6) (2012) 1099–1119.
[80] L. Ma, A.-L. Fauchille, P.J. Dowey, F.F. Pilz, L. Courtois, K.G. Taylor, P.D. Lee, Correlative multi-scale imaging of shales: A review and future perspectives, Geol. Soc. Lond. Spec. Publ. 454 (1) (2017) 175–199.
[81] K.E. Thompson, C.S. Willson, C.D. White, S. Nyman, J. Bhattacharya, A.H. Reed, Application of a new grain-based reconstruction algorithm to microtomography images for quantitative characterization and flow modeling, in: SPE Annual Technical Conference and Exhibition, Society of Petroleum Engineers, 2005.
[82] A. Sheppard, R. Sok, H. Averdunk, V. Robins, A. Ghous, Analysis of rock microstructure using high-resolution X-ray tomography, in: Proceedings of the International Symposium of the Society of Core Analysts, 2006, pp. 1–12.
[83] A. Rabbani, S. Jamshidi, S. Salehi, An automated simple algorithm for realistic pore network extraction from micro-tomography images, J. Pet. Sci. Eng. 123 (2014) 164–171.
[84] J.T. Gostick, Versatile and efficient pore network extraction method using marker-based watershed segmentation, Phys. Rev. E 96 (2) (2017) 023307.
[85] D. Silin, T. Patzek, Pore space morphology analysis using maximal inscribed spheres, Physica A 371 (2) (2006) 336–360.
[86] H. Dong, M.J. Blunt, Pore-network extraction from micro-computerized-tomography images, Phys. Rev. E 80 (3) (2009) 036307.
[87] A.S. Al-Kharusi, M.J. Blunt, Network extraction from sandstone and carbonate pore space images, J. Pet. Sci. Eng. 56 (4) (2007) 219–231.
[88] W.B. Lindquist, S.-M. Lee, D.A. Coker, K.W. Jones, P. Spanne, Medial axis analysis of void structure in three-dimensional tomographic images of porous media, J. Geophys. Res. Solid Earth 101 (B4) (1996) 8297–8310.
[89] W. Lindquist, A. Venkatarangan, Investigating 3D geometry of porous media from high resolution images, Phys. Chem. Earth A 24 (7) (1999) 593–599.
[90] R. Okuno, R. Johns, K. Sepehrnoori, A new algorithm for rachford-rice for multiphase compositional simulation, SPE J. 15 (02) (2010) 313–325.
[91] D.V. Voskov, H.A. Tchelepi, Comparison of nonlinear formulations for two-phase multi-component eos based simulation, J. Pet. Sci. Eng. 82 (2012) 101–111.
[92] Y. Wang, B. Yan, J. Killough, Compositional modeling of tight oil using dynamic nanopore properties, in: SPE Annual Technical Conference and Exhibition, Society of Petroleum Engineers, 2013.
[93] B. Nojabaei, N. Siripatrachai, R. Johns, T. Ertekin, Effect of saturation dependent capillary pressure on production in tight rocks and shales: A compositionally-extended black oil formulation, in: SPE Eastern Regional Meeting, Society of Petroleum Engineers, 2014.
[94] J. Jiang, R.M. Younis, Compositional modeling of enhanced hydrocarbons recovery for fractured shale gas-condensate reservoirs with the effects of capillary pressure and multicomponent mechanisms, J. Nat. Gas Sci. Eng. 34 (2016) 1262–1275.
[95] D.R. Sandoval, W. Yan, E.H. Stenby, Phase equilibrium in shale including porous media effects, in: Abu Dhabi International Petroleum Exhibition & Conference, Society of Petroleum Engineers, 2019.
[96] B. Bao, J. Feng, J. Qiu, S. Zhao, Direct measurement of minimum miscibility pressure of decane and CO2 in nanoconfined channels, ACS Omega (2020).
[97] P. Meakin, A.M. Tartakovsky, Modeling and simulation of pore-scale multiphase fluid flow and reactive transport in fractured and porous media, Rev. Geophys. 47 (3) (2009).
[98] L. Chen, J. Yu, H. Wang, Convex nanobending at a moving contact line: The missing mesoscopic link in dynamic wetting, Acs Nano 8 (11) (2014) 11493–11498.
[99] E.W.-H. Sun, I.C. Bourg, Molecular dynamics simulations of mineral surface wettability by water versus CO2: Thin films, contact angles, and capillary pressure in a silica nanopore, J. Phys. Chem. C (2020).
[100] Z. Li, Z. Jin, A. Firoozabadi, Phase behavior and adsorption of pure substances and mixtures and characterization in nanopore structures by density functional theory, SPE J. 19 (06) (2014) 1–096.
[101] T. Wu, H. Zhao, S. Tesson, A. Firoozabadi, Absolute adsorption of light hydrocarbons and carbon dioxide in shale rock and isolated kerogen, Fuel 235 (2019) 855–867.
[102] M. Mehana, Q. Kang, H. Nasrabadi, H. Viswanathan, Molecular modeling of subsurface phenomena related to petroleum engineering, Energy Fuels (2021).